Marte Pernille Hatlo Andresen

Inverse scattering of two-dimensional photonic structures

Marte Pernille Hatlo Andresen

Doctoral Thesis

NTNU – Trondheim
Norwegian University of
Science and Technology

NTNU – Trondheim
Norwegian University of
Science and Technology

NTNU

Marte Pernille Hatlo Andresen

Inverse scattering of two-dimensional photonic structures

Thesis for the degree of Philosophiae Doctor

Trondheim, February 2012

Norwegian University of Science and Technology
Faculty of Information Technology Mathematics
and Electrical Engineering
Department of Mathematical Sciences

NTNU – Trondheim
Norwegian University of
Science and Technology

PREFACE

This thesis is submitted in partial fulfillment of the requirements for the degree of Philosophiae Doctor (PhD) at the Norwegian University of Science and Technology (NTNU). The work has been carried out at the Department of Mathematical Sciences as part of the project "ICT and Mathematics", which aims to strengthen the theoretical research in information and communication technology at NTNU. The project is funded by NTNU, the Faculty of Information Technology, Mathematics and Electrical Engineering and the involved departments. My supervisors have been Prof. Harald E. Krogstad at the Department of Mathematical Sciences, Prof. Johannes Skaar at the Department of Electronics and Telecommunications and Dr. Larisa Beilina at the Department of Mathematical Sciences, Chalmers University of Technology and Gothenburg University.

The topic of my research has been the mathematics of periodic photonic structures. More precisely I have looked at mathematical methods for solving inverse problems connected to photonic crystals, and I have also contributed to a paper on perfect lenses. The work has resulted in four papers, three that are already published, and one that is submitted for publication. Paper I is concerned with gain saturation in perfect lenses. The other three papers are about inverse problems. Paper II uses a layer stripping approach to reconstruct the permittivity of a photonic crystal. The last two papers (paper III and IV) apply an adaptive finite element method to solve the same inverse problem as in paper II.

I am grateful for the opportunities I have been given to learn about mathematics and photonics, to do research, and to go to conferences and meet mathematicians and physicists. First of all, I would sincerely like to thank all three of my supervisors, Prof. Harald E. Krogstad, Prof. Johannes Skaar and Dr. Larisa Beilina, for giving me valuable guidance, encouragement and support. They have taught me a lot about mathematics, photonics and problem solving and helped me overcome the problems of interdisciplinary research.

My friends and colleagues at the department deserve warm thanks for a wonderful work environment and plenty of interesting discussions. In particular, I want to thank Hilde for sharing office and many nice conversations with me. I also want to thank the technical and administrative staff for always being helpful, and providing excellent computer facilities.

I am grateful to my family and friends for their patience and support. Special thanks to Mamma for all her help with the kids and the housework.

Finally, I would like to thank Christian, Jens and Ole for being the most important persons in my life. Christian's encouragement has been endless, without his support it would have been a lot harder to finish this thesis.

Marte Pernille Hatlo Andresen
Trondheim, December 2011

CONTENTS

Introduction

INTRODUCTION

The topic of this thesis is linked to research within photonics, with special emphasis on photonic crystals and materials with negative refraction. The main focus is on mathematical aspects of periodic photonic structures.

The usual way of constructing real photonic crystals is to carry out numerical simulations of electromagnetic waves hitting and being scattered off a trial design. The design is then changed by optimization or intuition until the structure has the desired properties. As a supplement to the forward simulations and the trial and error approach, we consider here the *inverse problem* where the structure is determined from observations of the scattered waves. The ultimate goal is being able to reconstruct the structures from the observations and use this as a supplementary tool for the design of structures with desired features.

The focus of the research is on the reconstruction of two-dimensional structures using data collected from scattered waves. Waves are predominantly thought of as electromagnetic waves and the structures as photonic crystals. However, the mathematical formulation as such has larger applicability. It has turned out that bringing this over from one-dimensional to two-dimensional structures meets considerable challenges, and the research focuses on two different approaches. The first approach is *layer stripping*, originally developed in geophysics, and the second is an adaptive technique to solve coefficient inverse problems (CIPs). The adaptive finite element method for solving CIPs has been developed by Dr. Larisa Beilina [6]. During the iteration process, the method applies a mesh adaptive finite element (FE) formulation.

Moreover, the transfer matrix method applied in the layer stripping method has also been used to study perfect lenses.

1. PHOTONIC CRYSTALS

Photonic crystals are periodic dielectric structures designed to affect electromagnetic waves in the visible light range [25, 49]. These structures may be viewed as the electromagnetic analogy of semiconductors. In solid state physics, semiconductors have been thoroughly studied. The periodic potential in a semiconductor is well known to have allowed and forbidden electronic energy bands. In much the same way, photonic crystal may have so-called photonic band gaps. There are frequency gaps where light is restricted from propagating through the structure. One distinguishes between one-, two- and three-dimensional structures, where the dimensions refer to whether the dielectric constant varies in one, two or three directions. However, only two- and three-dimensional structures are considered photonic crystals [52]. Since the basic physical phenomenon is diffraction, the periodicity of the photonic crystal must be of the same length scale as the wavelength of the electromagnetic waves [49]. There may seem to be a close connection between photonic crystals and X-ray crystal diffraction. However, there is a significant difference in the refractive index variations of the crystals. Whereas this variation is very small for X-rays, it is usually quite significant for photonic crystals [52]. Thus, a photonic

crystal is a two- or three-dimensional dielectric structure, with a significant contrast in the refractive index.

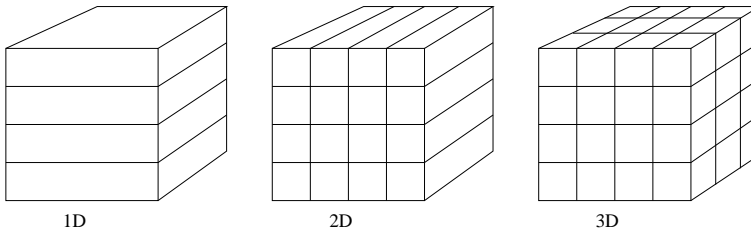1D   2D   3D

FIGURE 1. Simple examples of one- two- and three-dimensional photonic structures, where the dielectric constant is periodic along one, two or three axes.

One-dimensional structures have been studied since 1887. The pioneer work was done by Lord Rayleigh who studied how the reflected color from a crystalline mineral varies sharply with the angle [27, 40]. He thus discovered that multi-layered dielectric stacks have angle dependent band gaps. These one-dimensional structures are used in thin-film optics, such as reflecting coatings on lenses and color changing paints [49].

In 1987 Eli Yablonovich [51] and Sajeev John [26] published their first papers, which are considered the starting point for the field of photonic crystals. The papers address the possibility of photonic band gaps in two- and three-dimensions. Since then, the development of the field has grown quite fast. Due to fabrication challenges, the earliest studies were concerned with theory and structures in the microwave regime [49]. The scale invariance of Maxwell's equations makes it possible to construct and study structures on a greater length scale. The first three-dimensional band gap in the microwave regime was shown by Yablonovitch in 1991 [53]. The structure was built up by layers with holes, forming an inverse diamond structure. These structures are now known as Yablonovites. The first two-dimensional photonic crystal was produced in 1996 by Thomas Krauss [30].

As mentioned above, photonic crystals may have photonic band gap. Another possible advantage is that crystals can be used to trap and guide light. This is achieved by introducing defects in the periodic structure. Thus, photonic crystals can be used to guide light, and contrary to a fiber-optic cable, these structures may also have sharp bends [25]. Two-dimensional photonic crystals are available in the form of photonic crystal fibers. The three-dimensional counterparts, however, are far from commercialization.

Photonic crystals are also found in nature. The best known example is probably the opal stone. Other examples have been found in the wings of the M. rhetenor butterfly [47] and in the scales of the Brazilian beetle [21].

As the fabrication challenges are overcome, the ultimate goal would be to design photonic crystals with specific characteristics. Different methods for optimizing photonic structures have been proposed [23, 28], and a nice review can be found in [15].

2. Metamaterials

Metamaterials are artificial materials designed to have properties that can not be found in nature. Here we will focus on one type of metamaterials, namely those with negative index of refraction.

Let us first take a look at what negative refraction means. The index of refraction satisfies

$$(1) \qquad n^2 = \varepsilon\mu.$$

Thus the propagation of electromagnetic waves is determined by the dielectric constant ε and the magnetic permeability μ. If both the dielectric constant and the magnetic permeability are negative, it turns out that the refractive index becomes negative as well [45]. For a plane monochromatic wave all quantities in Maxwell's equations (Appendix A) are proportional to $e^{i(\mathbf{kx}-\omega t)}$, and the equations reduce to

$$(2) \qquad \begin{aligned} \mathbf{k} \times \mathbf{E} &= \omega\mu_0\mu\mathbf{H}, \\ \mathbf{k} \times \mathbf{H} &= -\omega\varepsilon_0\varepsilon\mathbf{E}. \end{aligned}$$

Furthermore, in a medium where $\varepsilon > 0$ and $\mu > 0$ the electric field $\mathbf{E}$, the magnetic field $\mathbf{H}$ and the wave vector $\mathbf{k}$ form a right-handed triplet of vectors. If, instead, we have $\varepsilon < 0$ and $\mu < 0$ the set of vectors will form a left-handed triplet. These media are sometimes referred to as "left-handed media". We also note that the Poynting vector $\mathbf{S} = \mathbf{E} \times \mathbf{H}$ will be in the opposite direction of the wave vector $\mathbf{k}$ for left-handed media. Consider a material with boundary parallel to the xy-plane and normal to the z-axis. The normal component of the Poynting vector must be continuous since there is no accumulation of energy at the boundary. This implies that the z-component of $\mathbf{k}_2$ in is negative. Moreover, from the boundary conditions for Maxwell's equations, stated in Appendix A, we know that the tangential components of the electric and magnetic fields are continuous. Thus, we must have phase match across the boundary. These two conditions mean that the incident wave projected on the boundary must propagate in the same direction as the projection from the refracted beam [43], and we find negative refraction, see Fig. 2.
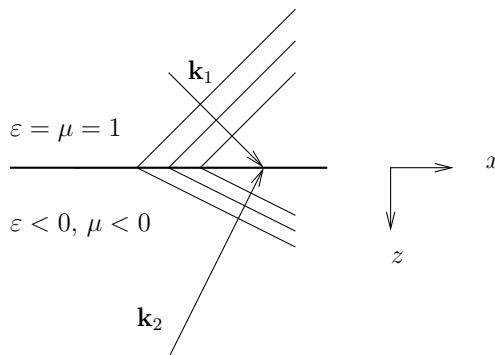
FIGURE 2. The figure shows the wave vectors and wavefronts as a wave is propagating into a material with $\varepsilon < 0$ and $\mu < 0$.

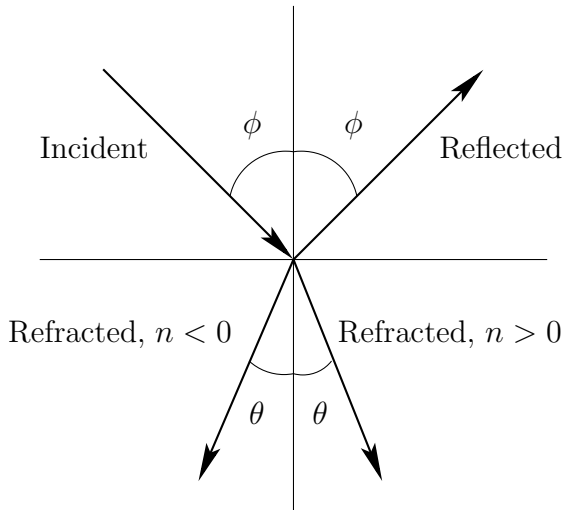The reflected and refractive rays are shown in Fig. 3.

FIGURE 3. An incident ray hits the boundary between two different media. The reflected ray is not affected by the sign of the refractive index n. However, for the refracted ray, we see that the z-component of the fields changes sign as the sign of n changes.

An interesting case occurs if medium 1 has $\varepsilon_1 > 0$ and $\mu_1 > 0$, while medium 2 has $\varepsilon_2 = -\varepsilon_1$ and $\mu_2 = -\mu_1$. In this case there is no reflected ray. Pendry used this fact to come up with the idea of a perfect lens [35]. A perfect lens is a slab of material with $n = -1$, see Figure 4. The main advantage of perfect lenses, compared to optical lenses, are their ability to focus light into an area that is smaller than the square of the wavelength. For optical lenses, this is not possible. The reason for this is that evanescent waves decay and thus are removed from the image. If we choose the z-axis to be axis of the lens, then propagating waves are limited by [35]

$$(3) \qquad\qquad k_x^2 + k_y^2 < \omega^2 c^{-2}.$$

The optical lens works by applying a phase correction to each of the Fourier components of the wave. The evanescent waves decay in amplitude, not in phase. However, it can be proved that a perfect lens cancels the decay of evanescent waves [35]. Thus in a perfect lens, both propagating and evanescent waves contribute to the resolution of the image.

Materials with negative refractive index are possible to fabricate, but the performance is unfortunately strongly limited by losses. Loss will limit the amplification of evanescent waves associated with large spatial frequencies, which will again limit the resolution [32,39]. One possible solution is to introduce gain into the metamaterials [17,20,29,34,37,38,41,42,46,55]. In this case, gain saturation is important, and must be taken into account when the resolution is calculated.
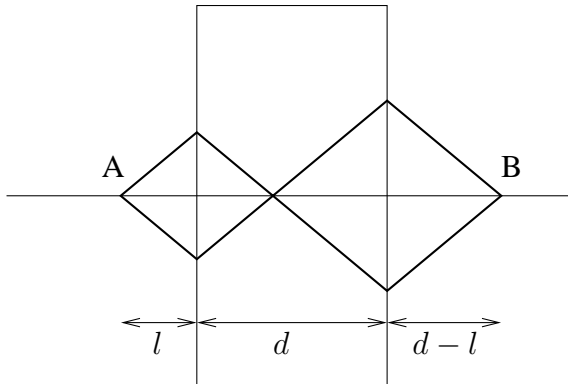
FIGURE 4. A ray of light passing through a perfect lens. Notice that it has two focus points, one inside the lens, and one at the back.

3. INVERSE PROBLEMS

Inverse problems appear in many different fields of physics and engineering, as, for example, medical imaging, seismology and geosciences. An inverse problem is concerned with determining causes for a desired or an observed effect [18]. The inverse problem is associated with a direct problem, which, as a rule, is simpler. The direct problem is important in itself, but is also needed to solve the inverse problem [15].

One huge research field of inverse problems is the field of inverse scattering. Problems arising in this field are concerned with the determination of the properties (as parameters and placement) of some hidden objects. To do this in a nondestructive way, one can measure the effect the unknown material has on an incident wave or particle. Then the inverse scattering problem consists of reconstructing the properties from the measured data, see Fig. 5. One well-known example of this is ultrasound.

Methods to solve inverse scattering problems are often based on asymptotic behavior of the scattered field. One example is an incident plane wave hitting a small object. In this case, the scattered wave will be approximately spherical far enough away from the object, and is called the far-field solution. On the other hand, the problems we have studied are concerned with near-field solutions. Consider a dielectric material. If the permittivity is known, the forward problem consists of computing the wave motion through the structure. Given instead scattering data from a known wave scattered by the structure, the inverse problem is to reconstruct the permittivity. Contrary to the far-field case mentioned above, here the periodicity of the unknown material is of the same size as the wavelength of the incident wave, and the data are measured close to structure. Those problems are also referred to as parameter identification problems.

Related to inverse problems are inverse design problems. Let us use design of photonic crystals as an example. It is, of course, preferable to know how the
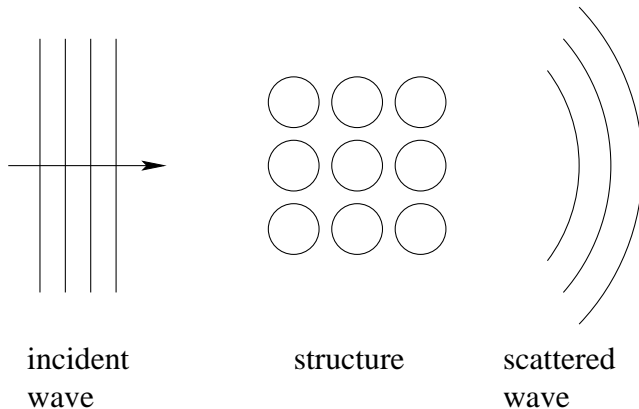
FIGURE 5. A simplified illustration of inverse scattering. An incident plane wave is scattered by some unknown structure.

photonic crystal should look to have certain properties. One way to obtain this is to change the structure by intuition or optimization, but it would be even better to state the desired data and be able to compute a crystal that produces this result. The inverse design problems may be treated as fictive inverse problems, where the desired data act as the observed data. However, for an inverse design problem to be solvable, one needs to start with a realizable response. The fictive response needs *e.g.* to be causal. Thus, this must also be taken into consideration.

Inverse problems tend to be ill-posed. Hadamard defined a problem to be well-posed if it fulfills the three following properties

(1) A solution exists
(2) The solution is unique
(3) The solution depends continuously on the data

For an inverse problem one, two or three of the properties may be violated. Being able to solve these problems requires some reformulation. First, violation of the second point is not always a problem. For inverse design, it is possibly even desirable to have several solutions to chose from. Otherwise, the non-uniqueness may be avoided by adding some extra requirements. Nonexistence of the solution may be treated by relaxing the definition of a solution. The last point is the one that most often fails to hold, and which also causes the most severe problems. Failure of this point, implies that small changes in the data will cause arbitrarily large changes in the solution. At last we note that even if a problem is well-posed, it may still be ill-conditioned [50], *i.e* small errors in the data can result in arbitrarily large errors in the result. To overcome this problem, the problem must be regularized.

The main idea of regularization is to replace the ill-posed problem by a regularized one that is well-posed. The regularized problem should be as close as possible to the problem at hand, while still a stable one. Thus, regularization is a compromise between accuracy and stability. Consider the equation

$$(4) \qquad\qquad\qquad Ax = y,$$

where we want to find x, given the operator A and the data y. As discussed above, we expect this inverse problem to be ill-posed, and the data y is usually given with some noise. Let y^δ be the "noisy data". Then the problem is to find a best-approximate solution $x^\dagger = A^\dagger y$, when only y^δ is known. Here, $A^\dagger$ is the Moore-Penrose generalized inverse [18] and $\|y^\delta - y\| \leq \delta$. To solve this, the unbounded operator $A^\dagger$ should be replaced by a parameter-dependent family $\{R_\alpha\}$ of continuous operators, such that $x^\dagger$ is approximated by $x_\alpha^\delta = R_\alpha y^\delta$. The operator must be chosen in such a way that x_α^δ depends continuously on the data y^δ, and so that if δ tends to zero, and α is appropriately chosen, then x_α^δ tends to $x^\dagger$. Note that here we have presented regularization for a linear operator, while the actual problems we have solved are non linear.

One commonly used type of regularization is the Tikhonov regularization, where the original problem is extended by some penalty term. Then the problem described above is solved by minimizing the functional

$$(5) \qquad\qquad J(x) = \|Ax - y\|^2 + \|Lx\|^2.$$

Minimizing Eq. (5) is thus a compromise between minimizing the residual norm, and keeping the penalty term $\|Lx\|$ small, which enforces stability [18]. A thorough description of properties and solution of Coefficient Inverse Problems (CIPs) may be found in Chapter 1 of [10].

4. Layer stripping

As discussed in Section 3, if we have data from an experiment where a plane wave hits a photonic structure, the associated inverse problem consists of reconstructing the unknown permittivity. To solve this problem, we have proposed two different methods. The first method is layer stripping. As the name implies, the method works by identifying the structure layer by layer. Layer stripping was first used to solve inverse acoustic problems for seismic data; overviews can be found in [14, 54]. Later, the method has also been applied to design and characterization of one-dimensional photonic crystal structures such as fiber Bragg gratings [44] and multimode structures [48].

Consider a two-dimensional structure, layered normal to the z-direction. The refractive index is varying in the x-direction, as well as the z-direction, but is constant with respect to y. The structure is probed by plane polarized harmonic electromagnetic waves traveling in the z-direction, with the electric field vector pointing in the y-direction. Given this structure, the *forward problem* consists of obtaining reflectance data for a known structure, while the *inverse problem* is to calculate the unknown properties, given the reflectance data.

The forward problem may be formulated in terms of transfer matrices. These matrices depend on the permittivity and the layer thickness. Thus, when the properties of the structure are known, it is straight forward to compute the reflection and transmission matrices for each layer as well as the whole structure.

The key step of the synthetic layer stripping algorithm is to combine reflectance data for different frequencies so as to synthesize data from a short pulse at the time the pulse hits the surface. The synthesized data may then be applied to reconstruct the refractive index profile in the top layer by identifying the local, time-domain Fresnel reflection at each point. Once the first layer is known, its transfer matrix may be computed, and the impact of the layer on the reflectance data eliminated,
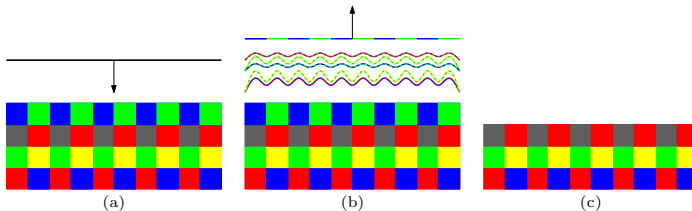
FIGURE 6. (a) An incident plane wave. (b) The wave is reflected
by the structure, note that the first reflections are only influenced
by the first layer. (c) The first part of the reflections is used to
calculate the properties of the top layer, and its effect may be
removed.

see Figure 6. The same idea is then applied to the modified reflectance data, and
continuing in the same way we are, at least in principle, able to reconstruct the
whole structure.

The layer stripping method is presented in full details in Paper II, which also
includes several numerical examples. From the numerical results, we see that we
are in fact able to reconstruct different structures consisting of several layers.

5. AN ADAPTIVE METHOD

Here we will discuss the second method which we have used to solve the inverse
problem consisting of reconstructing an unknown permittivity. This method is an
adaptive method. As this section also includes the proof of the *a posteriori* error
estimate, which is the basis of the adaptivity, we include a full description of the
method.

The mesh-adaptive method, developed in [5–9], was originally applied to acoustic
and elastic inverse scattering problems. Our main objective has been to adapt
the method to inverse electromagnetic scattering problems connected to photonic
crystals, *i.e.* to reconstruct an unknown dielectric permittivity. The basic technique
is to expose the structure with a known, time limited wave, and record the scattered
waves at some parts of the boundary of the domain. The error estimate is used
to localize regions where the error in the solution is largest, thus guiding where to
refine the finite element grid.

The application of the method to photonic crystals has required derivation and
proof of a new *a posteriori* error estimate for the Lagrangian, together with a
new numerical implementation, which now includes absorbing and mirror boundary
conditions. The derivation of the *a posteriori* estimate follows the main approach to
adaptive error control in computational differential equations, as presented in [3,6],
and references therein.

Our computational set-up consists of a domain of interest, with variations in the
dielectric permittivity, surrounded by homogeneous material. This enables us to
solve the wave equation with the hybrid FE(finite element)/FD(finite difference)
method developed in [13]. The method applies finite differences in the homoge-
neous surroundings, whereas finite elements are used where the material is hetero-
geneous. The method was chosen since it already existed and satisfied our needs.

The backscattering data are generated by a plane wave instead of a point source, as is often the case for real-life applications. Approximating the point source with a plane wave is reasonable when we assume that the point source is far from the domain where the dielectric function should be reconstructed. Based on this setting, we split the computational domain into two domains. In the surrounding (outer) domain we initialize the plane wave and assume that the value of the dielectric function is known. A finite difference method is used in this domain. In the inner domain, where the dielectric function should be reconstructed, we apply a finite element method together with the adaptive algorithm.

5.1. **The mathematical model and the forward problem.** The propagation of waves in an inhomogeneous and isotropic material is governed by the wave equation

$$(6) \qquad \Delta u = \frac{1}{c(x)^2} \frac{\partial^2 u}{\partial t^2}, \quad (x,t) \in \mathbb{R}^3 \times (0, \infty),$$

where $c(x)$ represents the wave speed. In the case of electromagnetic waves, the wave equation can be derived from Maxwell's equations, assuming that all functions are independent of one of the variables. The derivations can be found in Appendix B. Note that by assuming a nonmagnetic material, $c(x)$ depends only on the dielectric permittivity, ε, here scaled so that $c(x)^{-2} = \varepsilon(x)$.

Let $\Omega \subset \mathbb{R}^2$ be a bounded domain with a piecewise smooth boundary, $\partial\Omega = \partial\Omega_1 \cup \partial\Omega_2 \cup \partial\Omega_3$. Consider the forward problem given as

$$\varepsilon(x)\frac{\partial^2 u}{\partial t^2} - \Delta u = 0, \quad (x,t) \in \Omega \times (0,T),$$

$$u(x,0) = 0, \frac{\partial u}{\partial t}(x,0) = 0, \quad x \in \Omega,$$

$$(7) \qquad \partial_n u\big|_{\partial\Omega_1} = f(t), \text{ on } \partial\Omega_1 \times (0,T_1],$$

$$\partial_n u\big|_{\partial\Omega_1} = u_t, \text{ on } \partial\Omega_1 \times (T_1,T),$$

$$\partial_n u\big|_{\partial\Omega_2} = u_t, \text{ on } \partial\Omega_2 \times (0,T),$$

$$\partial_n u\big|_{\partial\Omega_3} = 0, \text{ on } \partial\Omega_3 \times (0,T).$$

Here $0 < T_1 < T$, T is the final time, and $f(t)$ a plane wave. Thus, the plane wave is initialized at the top boundary $\partial\Omega_1$ and propagates into Ω for $t \in (0,T_1]$. First order absorbing boundary conditions [19] are used on $\partial\Omega_1 \times (T_1,T)$ and $\partial\Omega_2 \times (0,T)$, and Neumann boundary conditions on both lateral boundaries, $\partial\Omega_3$, see Figure 7. The mirror boundary conditions on the left and right lateral boundaries, allow us to assume an infinite periodic space domain in the lateral direction.

The forward problem (Eq. (7)) is solved using the hybrid FE/FD method described in [13]. For this method, the domain Ω is split into a finite element domain Ω_{FEM} surrounded by a domain Ω_{FDM} with a structured mesh, $\Omega = \Omega_{\text{FDM}} \cup \Omega_{\text{FEM}}$. The space mesh in Ω_{FEM} consists of triangles and in Ω_{FDM} of squares, with mesh size $\tilde{h}$ in the overlapping regions.

Let the finite element mesh $K_h = \{K\}$ in Ω_{FEM} consist of triangular elements K. Let us associate with K_h a mesh function $h_K(x) = \text{diam}(K), \forall x \in K$, representing the diameter of the element K. For the time discretization, let $J_k = \{J\}$ be a partition of the time interval $I = (0,T)$ into time intervals $J = (t_{k-1}, t_k]$ of uniform length $\tau = t_k - t_{k-1}$.
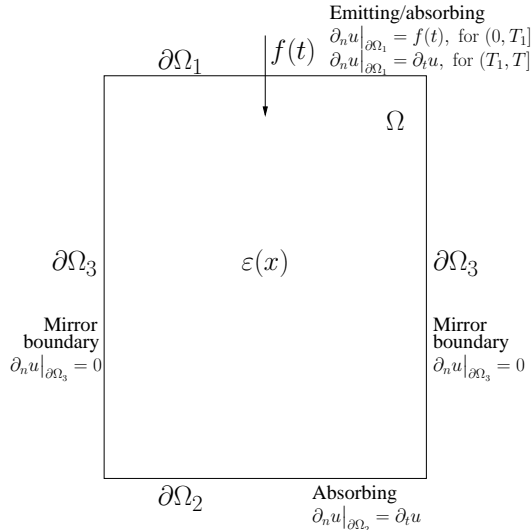
Emitting/absorbing
$\partial_n u\big|_{\partial\Omega_1} = f(t),\ \text{for }(0,T_1]$
$\partial_n u\big|_{\partial\Omega_1} = \partial_t u,\ \text{for }(T_1,T]$

$\partial\Omega_1$ $\Big| f(t)$

Ω

$\partial\Omega_3$ $\varepsilon(x)$ $\partial\Omega_3$

Mirror   Mirror
boundary   boundary
$\partial_n u\big|_{\partial\Omega_3} = 0$ $\partial_n u\big|_{\partial\Omega_3} = 0$

$\partial\Omega_2$ Absorbing
$\partial_n u\big|_{\partial\Omega_2} = \partial_t u$

FIGURE 7. Boundary conditions for the forward problem.

5.2. **The inverse problem.** The inverse problem for Eq. (7) is formulated as an optimization problem. Given observations u_{obs} at a finite set of points x_{obs}, the goal is to determine the coefficient $\varepsilon(x)$ for $x \in \Omega$, which minimizes the functional

$$(8) \qquad J(u,\varepsilon) = \frac{1}{2}\int_\Omega \int_0^T (u - u_{\text{obs}})^2 \delta_{\text{obs}}\ \mathrm{d}t\mathrm{d}x + \frac{1}{2}\gamma \int_\Omega (\varepsilon - \varepsilon_0)^2\ \mathrm{d}x.$$

Here $\delta_{\text{obs}} = \sum \delta(x - x_{\text{obs}})$ is a sum of delta-functions corresponding to the observation points. Moreover, γ is a regularization parameter, and ε_0 is the initial guess value for the unknown coefficient.

Denote

$$(9) \quad \begin{aligned}
H_u^2(\Omega \times (0,T)) &= \{f \in H^2(\Omega \times (0,T)) : f(x,0) = f_t(x,0) = 0\}, \\
H_u^1(\Omega \times (0,T)) &= \{f \in H^1(\Omega \times (0,T)) : f(x,0) = 0\}, \\
H_\lambda^2(\Omega \times (0,T)) &= \{f \in H^2(\Omega \times (0,T)) : f(x,T) = f_t(x,T) = 0\}, \\
H_\lambda^1(\Omega \times (0,T)) &= \{f \in H^1(\Omega \times (0,T)) : f(x,T) = 0\}, \\
U &= H_u^2(\Omega \times (0,T)) \times H_\lambda^2(\Omega \times (0,T)) \times C^2(\bar{\Omega}), \\
\bar{U} &= H_u^1(\Omega \times (0,T)) \times H_\lambda^1(\Omega \times (0,T)) \times L_2(\Omega),
\end{aligned}$$

where all functions are real valued. Hence, $U \subset \bar{U}$ and U is dense in $\bar{U}$.

In order to incorporate the constraint imposed by Eq. (7), we introduce the Lagrangian

$$
(10) \qquad L(v) = J(u, \varepsilon) + \int_0^T \int_\Omega \lambda \left(\varepsilon u_{tt} - \Delta u \right) \mathrm{d}x \mathrm{d}t,
$$

where λ is the Lagrange multiplier and $v = (u, \lambda, \varepsilon) \in U$. Clearly, if u is a solution of Eq. (7), then $L(v) = J(u, \varepsilon)$. Integration by parts in (10) leads to

$$
(11) \qquad
\begin{aligned}
L(v) = {} & J(u, \varepsilon) - \int_0^T \int_\Omega \varepsilon u_t \lambda_t \mathrm{d}x \mathrm{d}t + \int_0^T \int_\Omega \nabla u \nabla \lambda \mathrm{d}x \mathrm{d}t \\
& - \int_{T_1} \int_{\partial\Omega_1} u_t \lambda \mathrm{d}\sigma \mathrm{d}t - \int_0^T \int_{\partial\Omega_2} u_t \lambda \mathrm{d}\sigma \mathrm{d}t - \int_0^{T_1} \int_{\partial\Omega_1} f(t) \lambda \mathrm{d}\sigma \mathrm{d}t.
\end{aligned}
$$

A stationary point of the functional $L(v)$, satisfies

$$
(12) \qquad L'(v)(\bar{v}) = 0, \quad \forall \bar{v} = (\bar{u}, \bar{\lambda}, \bar{\varepsilon}) \in \bar{U},
$$

where $L'(v)(\cdot)$ is the Fréchet derivative of L at v. Here we will use an heuristic approach to find the Fréchet derivative. In this derivation we assume that the functions u, λ, and ε can be varied independently. However, when the Fréchet derivative is calculated, we assume that the solutions of the forward and adjoint problems depend on ε. A rigorous derivation of the Fréchet derivative, stating appropriate smoothness assumptions for the solutions of the state and adjoint problems, can be found in [12] and is far from trivial.

To find the gradient, one considers $L(v + \bar{v}) - L(v)$, $\forall \bar{v} \in \bar{U}$, and single out the linear part of this expression with respect to $\bar{v}$. Hence, from (11) and (12),

$$
(13) \qquad
\begin{aligned}
L'(v)(\bar{v}) = {} & \int_0^T \int_\Omega \bar{u}(u - u_{\mathrm{obs}}) \delta_{\mathrm{obs}} \mathrm{d}x \mathrm{d}t + \gamma \int_\Omega \bar{\varepsilon}(\varepsilon - \varepsilon_0) \mathrm{d}x \\
& - \int_0^T \int_\Omega \varepsilon(u_t \bar{\lambda}_t + \bar{u}_t \lambda_t) \mathrm{d}x \mathrm{d}t - \int_0^T \int_\Omega \bar{\varepsilon} u_t \lambda_t \mathrm{d}x \mathrm{d}t \\
& + \int_0^T \int_\Omega (\nabla u \nabla \bar{\lambda} + \nabla \bar{u} \nabla \lambda) \mathrm{d}x \mathrm{d}t - \int_{T_1} \int_{\partial\Omega_1} (u_t \bar{\lambda} + \bar{u}_t \lambda) \mathrm{d}\sigma \mathrm{d}t \\
& - \int_0^T \int_{\partial\Omega_2} (u_t \bar{\lambda} + \bar{u}_t \lambda) \mathrm{d}\sigma \mathrm{d}t - \int_0^{T_1} \int_{\partial\Omega_1} f(t) \bar{\lambda} \mathrm{d}\sigma \mathrm{d}t.
\end{aligned}
$$

Integration by parts in (13) now brings out $\bar{v}$,

$$
\begin{aligned}
L'(v)(\bar{v}) = &\int_0^T \int_\Omega \bar{\lambda}(\varepsilon u_{tt} - \Delta u)\mathrm{d}x\mathrm{d}t + \int_{T_1}^T \int_{\partial\Omega_1} \bar{\lambda}(\partial_n u - u_t)\mathrm{d}\sigma\mathrm{d}t \\
&+ \int_0^T \int_{\partial\Omega_2} \bar{\lambda}(\partial_n u - u_t)\mathrm{d}\sigma\mathrm{d}t + \int_0^{T_1} \int_{\partial\Omega_1} \bar{\lambda}(\partial_n u - f(t))\mathrm{d}\sigma\mathrm{d}t \\
&+ \int_0^T \int_\Omega \bar{u}((u - u_{\mathrm{obs}})\delta_{\mathrm{obs}} + \varepsilon\lambda_{tt} - \Delta\lambda)\mathrm{d}x\mathrm{d}t \\
&+ \int_{T_1}^T \int_{\partial\Omega_1} \bar{u}(\partial_n\lambda - \lambda_t)\mathrm{d}\sigma\mathrm{d}t + \int_0^T \int_{\partial\Omega_2} \bar{u}(\partial_n\lambda - \lambda_t)\mathrm{d}\sigma\mathrm{d}t \\
&+ \int_0^{T_1} \int_{\partial\Omega_1} \bar{u}\partial_n\lambda\mathrm{d}\sigma\mathrm{d}t + \int_0^T \int_{\partial\Omega_3} \bar{u}\partial_n\lambda\mathrm{d}\sigma\mathrm{d}t \\
&+ \int_\Omega \bar{\varepsilon} \left[\gamma(\varepsilon - \varepsilon_0) - \int_0^T u_t\lambda_t\mathrm{d}t \right] \mathrm{d}x.
\end{aligned}
$$

(14)

Hence, (12) and (13) imply that every integral term in Eq. (14) equals zero. Thus, if $(u, \lambda, \varepsilon) = v \in U$ is a minimizer of the Lagrangian $L(v)$ in (11), then the terms containing $\bar{\lambda}$ correspond to the forward problem (7). Furthermore, the terms with $\bar{u}$ are the weak form of the adjoint state equation,

$$
\begin{aligned}
&\varepsilon\lambda_{tt} - \Delta\lambda = -(u_{obs} - u)\delta_{\mathrm{obs}}, \quad (x,t) \in \Omega \times (0,T), \\
&\partial_n\lambda = 0 \text{ on } \partial\Omega_1 \times [0,T_1), \\
&\partial_n\lambda = \lambda_t \text{ on } \partial\Omega_1 \times [T_1,T), \\
&\partial_n\lambda = \lambda_t \text{ on } \partial\Omega_2 \times (0,T), \\
&\partial_n\lambda = 0 \text{ on } \partial\Omega_3 \times [0,T), \\
&\lambda(x,T) = \lambda_t(x,T) = 0, \quad x \in \Omega.
\end{aligned}
$$

(15)

At last, from the term involving $\bar{\varepsilon}$, we get

(16)
$$
\varepsilon = \frac{1}{\gamma} \int_0^T u_t\lambda_t\mathrm{d}t + \varepsilon_0, x \in \Omega,
$$

Thus, we can find ε from Eq. (16), where the functions $u \in H_u^1$ and $\lambda \in H_\lambda^1$ are weak solutions of the problems (7) and (15), respectively.

The boundary value problem (15) is solved backwards in time. Uniqueness and existence theorems for the initial/boundary value problems (7) and (15), including weak solutions, can be found in Chapter 4 of [31]. The Lagrangian $L(v)$ is minimized iteratively by obtaining weak solutions of the boundary value problems (7) and (15) on each step by a FEM formulation.

5.3. **A finite element method for the inverse problem.** To formulate the finite element method for (12), we introduce the finite element spaces $W_h^u \subset H_u^1(\Omega \times (0,T))$ and $W_h^\lambda \subset H_\lambda^1(\Omega \times (0,T))$ for u and λ, respectively. These spaces consist of continuous piecewise linear functions in space and time satisfying the initial conditions $u(x,0) = 0$ for $u \in W_h^u$, and $\lambda(x,T) = 0$ for $\lambda \in W_h^\lambda$. We also introduce the finite element space $V_h \subset L_2(\Omega)$ consisting of piecewise constant functions for the coefficient $\varepsilon(x)$ and denote $W_h^u \times W_h^\lambda \times V_h$ by U_h, $U_h \subset \bar{U}$. Thus, U_h is a discrete analogue of $\bar{U}$.

The FEM for (12) now consists of finding $v_h \in U_h$, so that

(17)
$$L'(v_h)(\bar{v}) = 0, \ \forall \bar{v} \in U_h.$$

We solve this using a quasi-Newton method, computing a sequence $\{\varepsilon_h^m\}_{m=1,\dots} \subset V_h$ of approximations to ε defined by the iteration

(18)
$$\varepsilon_h^{m+1}(x) = \varepsilon_h^m(x) - \alpha H^m g^m(x), m = 1, \dots$$

Here α is the step length computed by the line-search algorithm in [36], $g^m(x)$ is the gradient, and H^m an approximation to the inverse of the Hessian of L, updated by the BFGS formula

$$H^{m+1} = (I - d^m s^m y^{mT}) H^m (I - d^m y^m s^{mT}) + \rho s^m s^{mT}, \ m = 1, \dots$$

where

(19)
$$d^m = 1/(y^{mT} s^m)$$

and

$$y^m = g^{m+1} - g^m.$$

The corrections s^m in (19) are defined as $s^m = \varepsilon_h^{m+1} - \varepsilon_h^m$. In the computations, we use a version of the BFGS update formula with limited storage for the Hessian [33], where a finite number of corrections for the computed gradients and parameters in (19) are stored. The nodal values of the gradient $g^m(x)$ follows from (16),

(20)
$$g^m(x) = \gamma(\varepsilon_h^m - \varepsilon_0) - \int_0^T u_{ht}^m \lambda_{ht}^m \ dt.$$

The FEM solutions $u_h^m \in W_h^u$ and $\lambda_h^m \in W_h^\lambda$ are obtained by solving the boundary value problems (7) and (15) with $\varepsilon := \varepsilon_h^m$.

5.4. **An *a posteriori* error estimate for the Lagrangian.** We shall now discuss an *a posteriori* bound for the error of the finite element approximation of the function ε in terms of the residual error obtained in the reconstruction process. The residual error can be evaluated once the FEM solutions have been computed.

Let $v \in U$ be a minimizer of the Lagrangian L on the space $\bar{U}$, and v_h a minimizer of this functional on U_h. That is, v is a solution of (12) and v_h a solution of (17).

The basic goal of adaptive error control for the Lagrangian is to find a mesh with as few nodes as possible such that $|L(v) - L(v_h)| \leq tol$ for a given tolerance tol. In this section we present and prove an estimate for the difference $|L(v) - L(v_h)|$, and discuss how the estimate is used in an adaptive algorithm.

Since adaptivity is a locally convergent numerical method, we may assume that we work in a small neighborhood of the exact solution $v^* \in U$ of the full problem. This means that if ε^* is the exact solution of the inverse problem, then $u^* = u(\varepsilon^*)$ is the exact solution of (7), and $u^* - u_{obs}^* = 0$. Moreover, the solution of the adjoint

problem (15) is $\lambda(\varepsilon^*) = 0$. However, we can never get exact measurements u^*_{obs} since they always suffer from a certain noise level. Thus, we assume that

$$\|v - v^*\|_{\bar{U}} \leq \sigma, \tag{21}$$

where σ is sufficiently small. Here, $v = (u(\varepsilon), \lambda(\varepsilon), \varepsilon)$, and we call ε the regularized solution of the minimization problem (8).

Theorem 5.1. *Let $L(v) = L(u, \lambda, \varepsilon)$ be the Lagrangian as defined in (11), and let $L(v_h) = L(u_h, \lambda_h, \varepsilon_h)$ be the approximation of $L(v)$. Then the following representation holds for the error $e = L(v) - L(v_h)$:*

$$
\begin{aligned}
|e| \leq{} & \int_0^{T_1}\!\!\int_{\partial\Omega_1} R_{u_1}\sigma_\lambda \mathrm{d}\sigma\mathrm{d}t + \int_0^{T}\!\!\int_{\Omega} R_{u_2}\sigma_\lambda \mathrm{d}x\mathrm{d}t + \int_0^{T}\!\!\int_{\Omega} R_{u_3}\sigma_\lambda \mathrm{d}x\mathrm{d}t \\
& + \int_{T_1}^{T}\!\!\int_{\partial\Omega_1} R_{u_4}\sigma_\lambda \mathrm{d}\sigma\mathrm{d}t + \int_0^{T}\!\!\int_{\partial\Omega_2} R_{u_5}\sigma_\lambda \mathrm{d}\sigma\mathrm{d}t \\
& + \int_0^{T}\!\!\int_{\Omega} R_{\lambda_1}\sigma_u\delta_{\mathrm{obs}} \mathrm{d}x\mathrm{d}t + \int_0^{T}\!\!\int_{\Omega} R_{\lambda_2}\sigma_u \mathrm{d}x\mathrm{d}t + \int_0^{T}\!\!\int_{\Omega} R_{\lambda_3}\sigma_u \mathrm{d}x\mathrm{d}t \\
& + \int_0^{T}\!\!\int_{\partial\Omega_1} R_{\lambda_4}\sigma_u \mathrm{d}\sigma\mathrm{d}t + \int_0^{T}\!\!\int_{\partial\Omega_2} R_{\lambda_5}\sigma_u \mathrm{d}\sigma\mathrm{d}t \\
& + \int_0^{T}\!\!\int_{\Omega} R_{\varepsilon_1}\sigma_\varepsilon \mathrm{d}x\mathrm{d}t + \int_{\Omega} R_{\varepsilon_2}\sigma_\varepsilon \mathrm{d}x,
\end{aligned}
\tag{22}
$$

where the residuals are defined by

$$R_{u_1} = |f(t)|,\ \ R_{u_2} = \max_{S \subset \partial K} h_K^{-1}\big|\big[\partial_s u_h\big]\big|,$$
$$R_{u_3} = \varepsilon_h\tau^{-1}\big|\big[u_{ht}\big]\big|,\ \ R_{u_4} = R_{u_5} = |u_{ht}|,$$
$$R_{\lambda_1} = |u_h - u_{\mathrm{obs}}|,\ \ R_{\lambda_2} = \max_{S \subset \partial K} h_K^{-1}\big|\big[\partial_s \lambda_h\big]\big|,$$
$$R_{\lambda_3} = \varepsilon_h\tau^{-1}\big|\big[\lambda_{ht}\big]\big|,\ \ R_{\lambda_4} = R_{\lambda_5} = |\lambda_{ht}|,$$
$$R_{\varepsilon_1} = |\lambda_{ht}| \cdot |u_{ht}|,\ \ R_{\varepsilon_2} = \gamma|\varepsilon_h - \varepsilon_0|,$$

and the interpolation errors are

$$\sigma_\lambda = C\tau\,|[\lambda_{ht}]| + Ch_K\,|[\partial_n \lambda_h]|,$$
$$\sigma_u = C\tau\,|[u_{ht}]| + Ch_K\,|[\partial_n u_h]|,$$
$$\sigma_\varepsilon = C\big|[\varepsilon_h]\big|.$$

Here, $[v]$ denotes the maximum of the modulus of a jump of v across the face of an element K (or the boundary node of a time interval J), $\partial_s v$ denotes the normal derivative of v across a side of K, $\partial_n v$ denotes the derivative of v in the outward normal of an element K, $[v_t]$ is the maximum modulus of the jump of the time derivative of v across a boundary node of J, C is interpolation constants of moderate size.

Proof. Throughout the proof, let C denote different constants of a moderate size. As in [2], we use the fundamental theorem of calculus to write

$$
\begin{aligned}
e &= L(v) - L(v_h) \\
&= \int_0^1 \frac{\mathrm{d}}{\mathrm{d}s} L(v_h + s(v - v_h)) \mathrm{d}s \\
&= \int_0^1 L'(sv + (1-s)v_h)(v - v_h) \mathrm{d}s \\
&= L'(v_h)(v - v_h) + R,
\end{aligned}
$$

where $R = \mathcal{O}\left(\sigma^2\right)$. Since σ is small, we may ignore R in (24), see details in [1] and [12] for similar results in the case of a general nonlinear operator equation.

Neglecting the term R, and using the Galerkin orthogonality (17) with the splitting

$$
(23) \qquad\qquad v - v_h = (v - v_h^I) + (v_h^I - v_h),
$$

where $v_h^I \in U_h$ denotes an interpolant of v, leads to the following error representation:

$$
(24) \qquad\qquad e \approx L'(v_h)(v - v_h^I) = I_1 + I_2 + I_3.
$$

Here

$$
\begin{aligned}
I_1 = &-\int_0^T \int_\Omega \varepsilon_h u_{ht}(\lambda_t - \lambda_{ht}^I)\mathrm{d}x\mathrm{d}t + \int_0^T \int_\Omega \nabla u_h \nabla(\lambda - \lambda_h^I)\mathrm{d}x\mathrm{d}t \\
&-\int_0^{T_1} \int_{\partial\Omega_1} f(t)(\lambda - \lambda_h^I)\mathrm{d}\sigma\mathrm{d}t - \int_{T_1}^T \int_{\partial\Omega_1} u_{ht}(\lambda - \lambda_h^I)\mathrm{d}\sigma\mathrm{d}t \\
&-\int_0^T \int_{\partial\Omega_2} u_{ht}(\lambda - \lambda_h^I)\mathrm{d}\sigma\mathrm{d}t,
\end{aligned}
$$

$$
\begin{aligned}
I_2 = &\int_0^T \int_\Omega (u_h - u_{\text{obs}})(u - u_h^I)\delta_{\text{obs}}\mathrm{d}x\mathrm{d}t \\
&-\int_0^T \int_\Omega \varepsilon_h \lambda_{ht}(u_t - u_{ht}^I)\mathrm{d}x\mathrm{d}t + \int_0^T \int_\Omega \nabla\lambda_h \nabla(u - u_h^I)\mathrm{d}x\mathrm{d}t \\
&+\int_0^T \int_{\partial\Omega_1} \lambda_{ht}(u - u_h^I)\mathrm{d}\sigma\mathrm{d}t + \int_0^T \int_{\partial\Omega_2} \lambda_{ht}(u - u_h^I)\mathrm{d}\sigma\mathrm{d}t,
\end{aligned}
$$

$$
I_3 = -\int_0^T \int_\Omega \lambda_{ht} u_{ht}(\varepsilon - \varepsilon_h^I)\mathrm{d}x\mathrm{d}t + \gamma \int_\Omega (\varepsilon_h - \varepsilon_0)(\varepsilon - \varepsilon_h^I)\mathrm{d}x.
$$

To estimate I_1, we integrate by parts in the first and second terms to obtain:

$$
\begin{aligned}
|I_1| =| &\int_0^T \int_\Omega \varepsilon_h u_{htt}(\lambda - \lambda_h^I)\mathrm{d}x\mathrm{d}t - \int_0^T \int_\Omega \triangle u_h(\lambda - \lambda_h^I)\mathrm{d}x\mathrm{d}t \\
&- \int_0^{T_1} \int_{\partial\Omega_1} f(t)(\lambda - \lambda_h^I)\mathrm{d}\sigma\mathrm{d}t - \int_{T_1}^T \int_{\partial\Omega_1} u_{ht}(\lambda - \lambda_h^I)\mathrm{d}\sigma\mathrm{d}t \\
&- \int_0^T \int_{\partial\Omega_2} u_{ht}(\lambda - \lambda_h^I)\mathrm{d}\sigma\mathrm{d}t \\
&- \sum_k \int_\Omega \varepsilon_h \big[u_{ht}(t_k)\big](\lambda - \lambda_h^I)(t_k)\mathrm{d}x \\
&+ \sum_K \int_0^T \int_{\partial K} \partial_n u_h(\lambda - \lambda_h^I)\ \mathrm{d}\sigma\mathrm{d}t \big|.
\end{aligned}
$$

(25)

Here, $\big[u_{ht}(t_k)\big]$ denotes the jump of the derivative of u_h at time t_k (see Figure 9), and $\partial_n u_h$ denote the derivative of u_h in the outward normal direction n of the boundary ∂K of element K.

Since u_h is a piecewise linear function, the terms u_{htt} and $\triangle u_h$ in (25) disappear, and we get:

$$
\begin{aligned}
|I_1| =| &-\int_0^{T_1} \int_{\partial\Omega_1} f(t)(\lambda - \lambda_h^I)\mathrm{d}\sigma\mathrm{d}t - \int_{T_1}^T \int_{\partial\Omega_1} u_{ht}(\lambda - \lambda_h^I)\mathrm{d}\sigma\mathrm{d}t \\
&- \int_0^T \int_{\partial\Omega_2} u_{ht}(\lambda - \lambda_h^I)\mathrm{d}\sigma\mathrm{d}t \\
&- \sum_k \int_\Omega \varepsilon_h \big[u_{ht}(t_k)\big](\lambda - \lambda_h^I)(t_k)\mathrm{d}x \\
&+ \sum_K \int_0^T \int_{\partial K} \partial_n u_h(\lambda - \lambda_h^I)\mathrm{d}\sigma\mathrm{d}t \big|.
\end{aligned}
$$

(26)

In the last term of equation (26) we sum over the element boundaries, where each interior side $S \in S_h$ occurs twice, see Figure 8. Denoting by $\partial_{n\pm} u_h$ the derivative of u_h in the outward normal direction $n^\pm$ to element $K^\pm$, and by $\partial_s u_h$ the derivative of a function u_h in one of the normal directions, n^- and n^+, of each side S, we can write

(27)
$$
\sum_K \int_{\partial K} \partial_n u_h(\lambda - \lambda_h^I)\ \mathrm{d}\sigma = \sum_S \int_S \big[\partial_s u_h\big](\lambda - \lambda_h^I)\ \mathrm{d}\sigma,
$$

where the jump $\big[\partial_s u_h\big]$ is defined as

$$
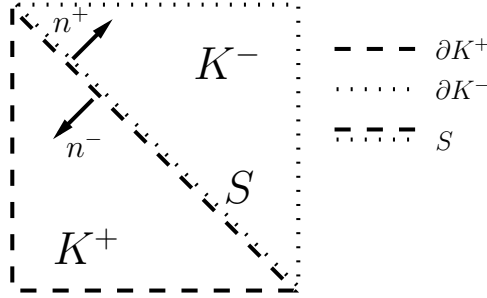[\partial_s u_h] = \max_{S \in \partial K} \{\partial_{n^+} u_h, \partial_{n^-} u_h\}.
$$

FIGURE 8. Two neighboring elements K^+ and K^-, their boundaries, ∂K^+ and ∂K^-, and the interior side S.

We distribute each jump equally to the two sharing elements and return to a sum of the element edges ∂K :

$$(28) \qquad \sum_S \int_S \left[\partial_s u_h\right](\lambda - \lambda_h^I) \, \mathrm{d}\sigma = \sum_K \frac{1}{2} \int_{\partial K} \left[\partial_s u_h\right](\lambda - \lambda_h^I) \, \mathrm{d}\sigma.$$

We multiply and divide by h_K, formally set $\mathrm{d}x = h_K \mathrm{d}\sigma$ and replace the integrals over the element boundaries ∂K by integrals over the elements K, to get:

$$(29) \qquad \begin{aligned} &\left| \sum_K \frac{1}{2} h_K^{-1} \int_{\partial K} \left[\partial_s u_h\right](\lambda - \lambda_h^I) \, h_K \, \mathrm{d}\sigma \right| \\ &\leq C \int_\Omega \max_{S \subset \partial K} h_K^{-1} \left| \left[\partial_s u_h\right] \right| \left| \lambda - \lambda_h^I \right| \, \mathrm{d}x, \end{aligned}$$

where $\left[\partial_s u_h\right]\big|_K = \max_{S \subset \partial K} \left[\partial_s u_h\right]\big|_S$.

In a similar way we can estimate the jump in time in (26) by multiplying and dividing by τ:

$$(30) \qquad \begin{aligned} &\left| \sum_k \int_\Omega \varepsilon_h \left[u_{ht}(t_k)\right] (\lambda - \lambda_h^I)(t_k) \, \mathrm{d}x \right| \\ &\leq \sum_k \int_\Omega \varepsilon_h \tau^{-1} \left| \left[u_{ht}(t_k)\right] \right| \left| (\lambda - \lambda_h^I)(t_k) \right| \, \tau \mathrm{d}x \\ &\leq C \sum_k \int_{J_k} \int_\Omega \varepsilon_h \tau^{-1} \left| \left[\partial_{t_k} u_h\right] \right| \left| \lambda - \lambda_h^I \right| \, \mathrm{d}x \mathrm{d}t \\ &= C \int_0^T \int_\Omega \varepsilon_h \tau^{-1} \left| \left[u_{ht}\right] \right| \left| (\lambda - \lambda_h^I) \right| \mathrm{d}x \mathrm{d}t. \end{aligned}$$

Here, we have defined $\left[\partial_{t_k} u_h\right]$ as the greatest of the two jumps on the interval (t_k, t_{k+1}): ,

$$\left[\partial_{t_k} u_h\right] = \max_k \left(\left[u_{ht}(t_k)\right], \; \left[u_{ht}(t_{k+1})\right] \right),$$

$$\left[u_{ht}\right] = \left[\partial_{t_k} u_h\right] \text{ on } J_k,$$

where $[u_{ht}(t_k)] = u_{ht}^+(t_k) - u_{ht}^-(t_k)$. The time jumps are illustrated in Figure 9.
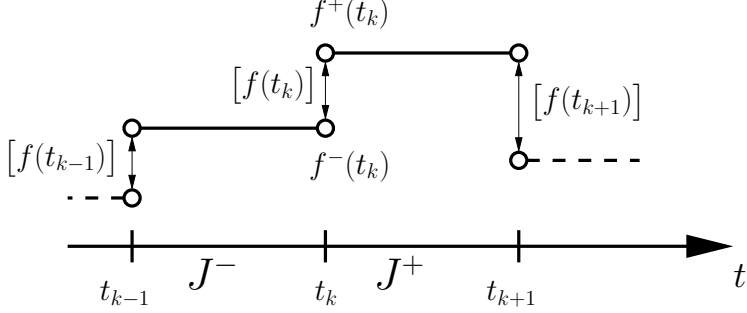

FIGURE 9. The jump of a function f on the time mesh.

We substitute the expressions (29) and (30) into (26), to get:

(31)
$$
\begin{aligned}
|I_1| \leq & \int_0^{T_1} \int_{\partial\Omega_1} |f(t)||\lambda - \lambda_h^I|\mathrm{d}\sigma\mathrm{d}t + \int_{T_1}^T \int_{\partial\Omega_1} |u_{ht}||\lambda - \lambda_h^I|\mathrm{d}\sigma\mathrm{d}t \\
& + \int_0^T \int_{\partial\Omega_2} |u_{ht}||\lambda - \lambda_h^I|\mathrm{d}\sigma\mathrm{d}t \\
& + C\int_0^T \int_\Omega \max_{S\subset\partial K} h_K^{-1}\big|[\partial_s u_h]\big||\lambda - \lambda_h^I|\,\mathrm{d}x\mathrm{d}t \\
& + C\int_0^T \int_\Omega \varepsilon_h\tau^{-1}\big|[u_{ht}]\big||\lambda - \lambda_h^I|\,\mathrm{d}x\mathrm{d}t.
\end{aligned}
$$

Next, we use the following standard interpolation estimate

(32)
$$|\lambda - \lambda_h^I| \leq C(\tau^2|\lambda_{tt}| + h_K^2|\lambda_{xx}|),$$

where we approximate the second derivative in time as

$$\lambda_{tt} = \frac{\partial^2\lambda}{\partial t^2} = \frac{\partial(\lambda_t)}{\partial t} \approx \frac{(\lambda_t)^+ - (\lambda_t)^-}{\tau} = \frac{[\lambda_{ht}]}{\tau}.$$

Here $(\cdot)^+$ and $(\cdot)^-$ represent values on two neighboring intervals J^+ and J^-, see Figure 9. In the same way we approximate the second derivative in space:

$$\lambda_{xx} \approx \frac{[\partial_n\lambda_h]}{h}.$$

Substituting both expressions above in (32), we obtain

(33)
$$|\lambda - \lambda_h^I| \leq C\big(\tau\big|[\lambda_{ht}]\big| + h_K\big|[\partial_n\lambda_h]\big|\big)$$

and the estimate for I_1 reduces to

$$
\begin{aligned}
|I_1| \leq C \int_0^{T_1} \int_{\partial\Omega_1} & |f(t)|(\tau|[\lambda_{ht}]| + h_K|[\partial_n\lambda_h]|)\mathrm{d}\sigma\mathrm{d}t \\
+ C \int_{T_1}^{T} \int_{\partial\Omega_1} & |u_{ht}|(\tau|[\lambda_{ht}]| + h_K|[\partial_n\lambda_h]|)\mathrm{d}\sigma\mathrm{d}t \\
+ C \int_0^{T} \int_{\partial\Omega_2} & |u_{ht}|(\tau|[\lambda_{ht}]| + h_K|[\partial_n\lambda_h]|)\mathrm{d}\sigma\mathrm{d}t \\
+ C \int_0^{T} \int_{\Omega} & \max_{S\subset\partial K} h_k^{-1}|[\partial_s u_h]|(\tau|[\lambda_{ht}]| + h_K|[\partial_n\lambda_h]|)\mathrm{d}x\mathrm{d}t \\
+ C \int_0^{T} \int_{\Omega} & \varepsilon_h\tau^{-1}|[u_{ht}]|(\tau|[\lambda_{ht}]| + h_K|[\partial_n\lambda_h]|)\mathrm{d}x\mathrm{d}t.
\end{aligned}
\tag{34}
$$

We estimate I_2 similarly as I_1. First, we integrate by parts to obtain

$$
\begin{aligned}
|I_2| \leq \Big| \int_0^{T} \int_{\Omega} & u_h - u_{\mathrm{obs}}(u - u_h^I)\delta_{\mathrm{obs}}\mathrm{d}x\mathrm{d}t + \int_0^{T} \int_{\Omega} \varepsilon_h\lambda_{htt}(u - u_h^I)\mathrm{d}x\mathrm{d}t \\
- \int_0^{T} \int_{\Omega} & \triangle\lambda_h(u - u_h^I)\mathrm{d}x\mathrm{d}t + \int_0^{T} \int_{\partial\Omega_1} \lambda_{ht}(u - u_h^I)\mathrm{d}\sigma\mathrm{d}t \\
+ \int_0^{T} \int_{\partial\Omega_2} & \lambda_{ht}(u - u_h^I)\mathrm{d}\sigma\mathrm{d}t\Big| \\
+ C \int_0^{T} \int_{\Omega} & \max_{S\subset\partial K} h_K^{-1}|[\partial_s\lambda_h]||u - u_h^I|\mathrm{d}x\mathrm{d}t \\
+ C \int_0^{T} \int_{\Omega} & \varepsilon_h\tau^{-1}|[\lambda_{ht}]||u - u_h^I|\mathrm{d}x\mathrm{d}t.
\end{aligned}
\tag{35}
$$

Since λ_h is piecewise linear, the terms with $\triangle \lambda_h$ and λ_{htt} will disappear:

$$
\begin{aligned}
\left| I_2 \right| \leq & \int_0^T \int_\Omega \left| u_h - u_{\text{obs}} \right| \left| u - u_h^I \right| \delta_{\text{obs}} \mathrm{d}x \mathrm{d}t \\
& + \int_0^T \int_{\partial\Omega_1} \left| \lambda_{ht} \right| \left| u - u_h^I \right| \mathrm{d}\sigma \mathrm{d}t \\
& + \int_0^T \int_{\partial\Omega_2} \left| \lambda_{ht} \right| \left| u - u_h^I \right| \mathrm{d}\sigma \mathrm{d}t \\
& + C \int_0^T \int_\Omega \max_{S \subset \partial K} h_K^{-1} \left| \left[\partial_s \lambda_h \right] \right| \left| u - u_h^I \right| \mathrm{d}x \mathrm{d}t \\
& + C \int_0^T \int_\Omega \varepsilon_h \tau^{-1} \left| \left[\lambda_{ht} \right] \right| \left| u - u_h^I \right| \mathrm{d}x \mathrm{d}t.
\end{aligned}
\tag{36}
$$

Next, we use the same kind of interpolation estimate for $\left| u - u_h^I \right|$ as we found for $\left| \lambda - \lambda_h^I \right|$ in equation (33), to get:

$$
\begin{aligned}
\left| I_2 \right| \leq & C \int_0^T \int_\Omega \left| u_h - u_{\text{obs}} \right| \left(\tau \left| \left[u_{ht} \right] \right| + h_K \left| \left[\partial_n u_h \right] \right| \right) \delta_{\text{obs}} \mathrm{d}x \mathrm{d}t \\
& + C \int_0^T \int_{\partial\Omega_1} \left| \lambda_{ht} \right| \left(\tau \left| \left[u_{ht} \right] \right| + h_K \left| \left[\partial_n u_h \right] \right| \right) \mathrm{d}\sigma \mathrm{d}t \\
& + C \int_0^T \int_{\partial\Omega_2} \left| \lambda_{ht} \right| \left(\tau \left| \left[u_{ht} \right] \right| + h_K \left| \left[\partial_n u_h \right] \right| \right) \mathrm{d}\sigma \mathrm{d}t \\
& + C \int_0^T \int_\Omega \max_{S \subset \partial K} h_K^{-1} \left| \left[\partial_s \lambda_h \right] \right| \left(\tau \left| \left[u_{ht} \right] \right| + h_K \left| \left[\partial_n u_h \right] \right| \right) \mathrm{d}x \mathrm{d}t \\
& + C \int_0^T \int_\Omega \varepsilon_h \tau^{-1} \left| \left[\lambda_{ht} \right] \right| \left(\tau \left| \left[u_{ht} \right] \right| + h_K \left| \left[\partial_n u_h \right] \right| \right) \mathrm{d}x \mathrm{d}t.
\end{aligned}
\tag{37}
$$

To estimate I_3 we use the following approximation estimate for $\varepsilon - \varepsilon_h^I$:

$$
\left| \varepsilon - \varepsilon_h^I \right| \leq C h_K \partial_x \varepsilon \leq C h_K \left| \frac{\left[\varepsilon_h \right]}{h_K} \right| \leq C \left| \left[\varepsilon_h \right] \right|,
\tag{38}
$$

and we end up with

$$
\left| I_3 \right| \leq \int_0^T \int_\Omega \left| \lambda_{ht} \right| \left| u_{ht} \right| \left| \left[\varepsilon_h \right] \right| \mathrm{d}x \mathrm{d}t + \gamma \int_\Omega \left| \varepsilon_h - \varepsilon_0 \right| \cdot \left| \left[\varepsilon_h \right] \right| \mathrm{d}x,
$$

which completes the proof.

□

Numerical experiments in paper III and IV, together with other publications [8,12] show that the dominating contribution to the error in the Lagrangian occurs in the residuals of the reconstruction of ε, which may be estimated from the above by

$$(39) \qquad \gamma \max_{\overline{\Omega}} |\varepsilon_h - \varepsilon_0| + \max_{\overline{\Omega}} \int_0^T |u_{ht}\lambda_{ht}| \, \mathrm{d}t.$$

While the integral terms in the *a posteriori* error for the Lagrangian were ignored due to numerical observations in the publications cited above, this fact was analytically explained in [11]. Thus, the error in the Lagrangian may be decreased by refining the grid locally in the regions where the absolute value of the gradient with respect to ε attains its maximum.

It was shown in [12] that the mesh refinement improves the accuracy of the regularized solution as long as the modulus of the gradient of the Tikhonov functional is not too small. This was consistently observed in [4,5,8,9], and also in papers III and IV.

5.5. **The adaptive algorithm.** Finally, we present an algorithm for the adaptive method.

Step 0. Choose an initial mesh K_h in the domain Ω and a time partition J_τ of the time interval $(0, T)$. Start with the initial approximation $\varepsilon_h^0 := \varepsilon_0$ and compute the sequence of functions ε_h^m in the steps described below.

Step 1. Compute FEM solutions $u_h(x, t, \varepsilon_h^m), \lambda_h(x, t, \varepsilon_h^m)$ of the state and adjoint problems (7), (15) on K_h, J_τ.

Step 2. Update the coefficient $\varepsilon := \varepsilon_h^{m+1}$ on K_h using (18).

Step 3. Stop computing the functions ε_h^m if either $\|g^m\|_{L_2(\Omega)} \le \theta$, or the norms $\|g^m\|_{L_2(\Omega)}$ abruptly grow, or the norms $\|g^m\|_{L_2(\Omega)}$ are stabilized, where $0 < \theta < 1$ is chosen by the user. Otherwise, set $m := m + 1$ and go to Step 1.

Step 4. Compute the function $A(x) = |g_h^m(x)|$. Refine the mesh where

$$(40) \qquad A(x) \ge \beta \max_{\overline{\Omega}} A(x).$$

Here, the tolerance number β is chosen by the user.

Step 5. Construct a new mesh K_h and a new time partition J_τ of the time interval $(0, T)$. The new time step τ of J_τ should satisfy the CFL (Courant-Friedrichs-Lewy) condition. Interpolate the initial approximation ε_h^0 on the new mesh. Return to Step 1 and perform all the steps above on the new mesh.

Step 6. Stop the mesh refinements when the stopping criterion described in Step 3 is satisfied.

6. Summary of the papers

6.1. **Paper I.**

Effect of gain saturation in a gain compensated perfect lens. In Paper I we develop a method for calculating the transmission, reflection, and detailed field profile of a gain compensated perfect lens. In particular, the impact of gain saturation is included in the analysis, and a method for calculating the fields of such nonlinear systems is developed. Gain saturation clearly improves the resolution of perfect lenses. However, gain saturation also results in non ideal effects, *e.g.* limited resolution and reflections. Moreover, the resolution associated with the lens is strongly dependent on the saturation constant of the active medium.

Since gain saturation is a nonlinear effect, different waves traversing the lens at the same time will interact through the material. Waves with a spatial frequency close to the resolution limit will have the greatest impact. As a rule of thumb, it is enough to know the sum of amplitudes of the waves at the source, and then assume that the mode with the largest spatial frequency has this amplitude. If this single wave is transmitted, in the sense of a transmission larger than $1/2$, then so will any superposition of waves with less spatial frequencies and the same sum of amplitudes.

For a non-compensated lens and TM polarization, the maximum spatial frequency resolved by the lens is approximately $-\frac{1}{d} \ln \frac{|1+\epsilon|}{2}$ [32, 39], where d is the thickness of the lens. Thus, for a fixed d, an exponential decrease in the losses is necessary to increase the resolution linearly. From our numerical results, a similar relation is approximately valid for the saturation constant of a gain compensated medium; to achieve a linear improvement in the resolution, the saturation constant must increase exponentially. This clearly shows the difficulties of achieving very high resolution.

Together with Johannes Skaar, I worked out the details in the two-dimensional transfer matrix method. Based on the theory, and an old implementation of the corresponding one-dimensional matrix method, I have implemented the numerical method, and produced all results presented in the paper.

6.2. **Paper II.**

Inverse scattering of two-dimensional photonic structures by layer stripping. In Paper II we present a layer stripping method for reconstructing 2d photonic structures. Layer stripping is based on causality, where the earliest scattered light is used to recover the structure layer by layer. Our setup is a 2D layered nonmagnetic structure probed by plane-polarized harmonic waves entering orthogonal to the layers. It is assumed that the dielectric permittivity in each layer only varies orthogonal to the polarization. Based on obtained reflectance data covering a suitable frequency interval, time-localized pulse data are synthesized and applied to reconstruct the refractive index profile in the leftmost layer by identifying the local, time-domain Fresnel reflection at each point. Once the first layer is known, its impact on the reflectance data is stripped off and the procedure is repeated for the next layer. In principle, the reconstruction is exact, and we have shown through numerical examples that we are able to reconstruct different structures consisting of several layers. The impact of evanescent modes and limited bandwidth is discussed.

There are essentially three fundamental mechanisms that limit the accuracy in practice: The presence of evanescent modes, accumulated reflection, and limited bandwidth. The fact that evanescent modes lead to inaccuracies means that either the probing frequencies must be sufficiently high, or the spatial transversal frequencies of the structure must be sufficiently small. The second limitation is a result of the fact that if the transmission through the structure is too small, little light reaches the back end. Then the back end has little influence on the reflection spectrum, and cannot be reconstructed accurately. Finally, the bandwidth must be sufficiently large such that the synthetic, incident pulse is shorter than the round-trip time in all layers. Alternatively, for a fixed available bandwidth the structure must vary sufficiently slowly in the longitudinal direction z.

The idea of using layer stripping to solve the inverse problem for photonic crystals came from Johannes Skaar. Together with him and Harald E. Krogstad, I have worked out the details in the layer stripping method. I carried out the numerical implementation of the method, and produced all the numerical examples in the paper.

6.3. **Paper III.**

Adaptive algorithms for an inverse electromagnetic scattering problem. In Paper III we present two different adaptive algorithms for an inverse electromagnetic scattering problem. The basis for the adaptive algorithms is an *a posteriori* error estimate, which is presented in the paper.

The inverse problem is formulated as an optimal control problem, where we solve equations expressing stationarity of an associated Lagrangian. The *a posteriori* error estimate for the Lagrangian couples residuals of the computed solution to weights of the reconstruction. We show that the weights can be obtained by solving an associated linearized problem for the Hessian of the Lagrangian, which is used in the second algorithm, while in the first algorithm we compute only the residuals. The performance of the adaptive finite element method and the usefulness of the *a posteriori* error estimate are illustrated in numerical examples.

For this paper I worked out the details in the proof of the *a posteriori* error estimate. The proof is not included in the paper, but is given in full in Sec. 5.4. I also did some numerical tests, although none of them are include in the paper.

6.4. **Paper IV.**

Reconstruction of dielectrics in a symmetric structure via adaptive algorithm with backscattering data. In Paper IV we formulate an adaptive algorithm and present numerical results for the adaptive reconstruction of the dielectric constant in a symmetric structure, given backscattering data from a single measurement. In the adaptive algorithm presented here we use an *a posteriori* error estimate for the Lagrangian applied to the regularized solution of the Coefficient Inverse Problem (CIP). To find the error in the Lagrangian we use its Fréchet derivative. We refine the mesh in all subdomains of the computational domain where the Fréchet derivative of the Lagrangian attains its maximal values. Our main objective has been to apply the adaptive finite element method to solve the electromagnetic CIP connected to photonic crystals, *i.e.* to reconstruct an unknown dielectric permittivity from backscattering data. The basic technique is to expose the structure with a known, time limited wave, and then record the backscattering waves. To solve the

CIP we use the hybrid FE/FD method developed in [13]. The numerical tests have consistently demonstrated accurate reconstruction of the locations and contrasts of the dielectric permittivity in the symmetric structure from the backscattering data using the adaptive algorithm outlined in the paper. In a second example we show that a locally convergent quasi-Newton works well when a good approximation to the exact solution is available, but performs poorly when a good initial guess is unavailable.

As for Paper III, the adaptivity in Paper IV is based on the *a posteriori* error estimate presented in Sec. 5.4. I also did the numerical tests presented in Example 1, Test 1.

Appendix

Appendix A. Maxwell's equations

The work presented in this thesis is related to photonic crystals and materials with negative refraction. These topics are concerned with electromagnetic waves propagating in some dielectric material. All macroscopic electromagnetism, including the propagation of electromagnetic waves, are governed by Maxwell's equations

$$
\tag{41} \nabla \times \mathbf{E}(\mathbf{x}, t) + \frac{\partial \mathbf{B}(\mathbf{x}, t)}{\partial t} = 0,
$$

$$
\tag{42} \nabla \times \mathbf{H}(\mathbf{x}, t) - \frac{\partial \mathbf{D}(\mathbf{x}, t)}{\partial t} = \mathbf{j},
$$

$$
\tag{43} \nabla \cdot \mathbf{D}(\mathbf{x}, t) = \rho,
$$

$$
\tag{44} \nabla \cdot \mathbf{B}(\mathbf{x}, t) = 0,
$$

in space, $\mathbf{x} = (x, y, z)$, and time, t. Here, $\mathbf{E}$ and $\mathbf{H}$ are the electric and magnetic fields, whereas $\mathbf{D}$ and $\mathbf{B}$ are the electric and magnetic flux densities, ρ is the free charges and $\mathbf{j}$ free currents.

Now we will focus on propagation in dielectric medium with no free particles or currents, $\rho =$ and $\mathbf{j} = 0$. Thus, light can propagate in the structure, but there are no sources of light. Furthermore, we assume the material to be linear, lossless, isotropic and time invariant, with no dispersion or spacial dispersion, in which case we have $\mathbf{D} = \varepsilon_0 \varepsilon \mathbf{E}$ and $\mathbf{B} = \mu_0 \mu \mathbf{H}$ [24]. Here ε_0 and μ_0 are the vacuum permittivity and permeability, while ε and μ are the relative permittivity and permeability. Given these assumptions, Maxwell's equations reduce to

$$
\tag{45} \nabla \times \mathbf{E}(\mathbf{x}, t) + \mu_0 \mu(\mathbf{x}) \frac{\partial \mathbf{H}(\mathbf{x}, t)}{\partial t} = 0,
$$

$$
\tag{46} \nabla \times \mathbf{H}(\mathbf{x}, t) - \varepsilon_0 \varepsilon(\mathbf{x}) \frac{\partial \mathbf{E}(\mathbf{x}, t)}{\partial t} = 0,
$$

$$
\tag{47} \nabla \cdot [\varepsilon(\mathbf{x}) \mathbf{E}(\mathbf{x}, t)] = 0,
$$

$$
\tag{48} \nabla \cdot [\mu(\mathbf{x}) \mathbf{H}(\mathbf{x}, t)] = 0.
$$

Across the material boundaries the following conditions need to be fulfilled [22]:

$$
\tag{49} \varepsilon_1 \mathbf{E}_1^\perp = \varepsilon_2 \mathbf{E}_2^\perp,
$$

$$
\tag{50} \mu_1 \mathbf{H}_1^\perp = \mu_2 \mathbf{H}_2^\perp,
$$

$$
\tag{51} \mathbf{E}_1^\parallel = \mathbf{E}_2^\parallel,
$$

$$
\tag{52} \mathbf{H}_1^\parallel = \mathbf{H}_2^\parallel.
$$

Here $\perp$ denotes the component normal to, and $\parallel$ the component parallel to the boundary. Regarding photonic crystals, most interesting materials have relative magnetic permeability close to unity, thus $\mathbf{B} = \mu_0 \mathbf{H}$. With this extra assumption,

Maxwell's equations are further reduced to

$$\nabla \times \mathbf{E}(\mathbf{x}, t) + \mu_0 \frac{\partial \mathbf{H}(\mathbf{x}, t)}{\partial t} = 0 \tag{53}$$

$$\nabla \times \mathbf{H}(\mathbf{x}, t) - \varepsilon_0 \varepsilon(\mathbf{x}) \frac{\partial \mathbf{E}(\mathbf{x}, t)}{\partial t} = 0 \tag{54}$$

$$\nabla \cdot [\varepsilon(\mathbf{x}) \mathbf{E}(\mathbf{x}, t)] = 0 \tag{55}$$

$$\nabla \cdot \mathbf{H}(\mathbf{x}, t) = 0. \tag{56}$$

APPENDIX B. DERIVATION OF THE WAVE EQUATION

Consider the propagation of an electromagnetic field in $\mathbb{R}^3$. Let $\mathbf{E}(x, t) = (E_1, E_2, E_3)$ and $\mathbf{H}(x, t) = (H_1, H_2, H_3)$, $x \in \Omega$, $t > 0$, be vectors of the electric and magnetic fields, respectively. We assume that the dielectric permittivity, $\varepsilon(x)$, is scalar and that the material is non-magnetic, so that $\mu(x) = 1$. The current density, $\mathbf{j}$, and the charge density, ρ, are both assumed to be zero. Consider the system of Maxwell's equations,

$$\nabla \times \mathbf{H} = \varepsilon \frac{\partial \mathbf{E}}{\partial t}, \tag{57}$$

$$\nabla \times \mathbf{E} = -\frac{\partial \mathbf{H}}{\partial t}, \tag{58}$$

and assume that all functions in (57)–(58) are independent of z, see [16]. Then (57)–(58) are equivalent to

$$\mathbf{i} \frac{\partial H_3}{\partial y} - \mathbf{j} \frac{\partial H_3}{\partial x} + \mathbf{k}(\frac{\partial H_2}{\partial x} - \frac{\partial H_1}{\partial y}) = \varepsilon(\mathbf{i} \frac{\partial E_1}{\partial t} + \mathbf{j} \frac{\partial E_2}{\partial t} + \mathbf{k} \frac{\partial E_3}{\partial t}), \tag{59}$$

$$\mathbf{i} \frac{\partial E_3}{\partial y} - \mathbf{j} \frac{\partial E_3}{\partial x} + \mathbf{k}(\frac{\partial E_2}{\partial x} - \frac{\partial E_1}{\partial y}) = -\mathbf{i} \frac{\partial H_1}{\partial t} - \mathbf{j} \frac{\partial H_2}{\partial t} - \mathbf{k} \frac{\partial H_3}{\partial t}, \tag{60}$$

and, in particular,

$$\varepsilon \frac{\partial E_3}{\partial t} = \frac{\partial H_2}{\partial x} - \frac{\partial H_1}{\partial y}, \tag{61}$$

$$\frac{\partial H_2}{\partial t} = \frac{\partial E_3}{\partial x}, \tag{62}$$

$$\frac{\partial H_1}{\partial t} = -\frac{\partial E_3}{\partial y}. \tag{63}$$

Differentiating (61) with respect to t, and inserting (62) and (63), we obtain

$$\varepsilon \frac{\partial^2 E_3}{\partial t^2} = \Delta E_3. \tag{64}$$

Equations (61)–(63) contain the variables H_1, H_2 and E_3 and are called the transverse electric (TE) polarization [16].

REFERENCES

[1] A. B. Bakushinsky and M. Yu. Kokurin. *Iterative Methods for Approximate Solution of Inverse Problems*. Springer, Dordrecht, 2004.

[2] R. Becker. Adaptive finite elements for optimal control problems. *Habilitationsschrift*, 2004.

[3] R. Becker and R. Rannacher. An optimal control approach to a posteriori error estimation in finite element methods. *Acta Numerica, Cambridge University Press*, 10:1–102, 2001.

[4] L. Beilina. Adaptive finite element/difference method for inverse elastic scattering waves. *Appl. Comput. Math.*, 1(2):158–174, 2002.

[5] L. Beilina. Adaptive hybrid FEM/FDM methods for inverse scattering problems. *J. Inverse Problems and Information Technologies*, 1(3):73–116, 2002.

[6] L. Beilina. *Adaptive Finite Element/Difference Methods for Time-Dependent Inverse Scattering Problems*. PhD thesis, Chalmers University of Technology and Göteborg University, 2003.

[7] L. Beilina. Adaptive hybrid finite element/difference methods: application to inverse elastic scattering. *J. Inv. Ill-Posed Problems*, 11(6):585–618, 2003.

[8] L. Beilina and C. Clason. An adaptive hybrid FEM/FDM method for an inverse scattering problem in scanning acoustic microscopy. *SIAM J. Sci. Comput.*, 28(1):382–402, 2006.

[9] L. Beilina and C. Johnson. A posteriori error estimation in computational inverse scattering. *Mathematical models and methods in applied sciences*, 15(1):23–37, 2005.

[10] L. Beilina and M. V. Klibanov. *Global Convergence and Adaptivity for Inverse Problems*. Springer-Verlag New York Inc, 2012.

[11] L. Beilina, M. V. Klibanov, and A. Kuzhuget. New a posteriori error estimates for adaptivity technique and global convergence for the hyperbolic coefficient inverse problem. *Journal of Mathematical Sciences*, 172(4):449–476, 2011.

[12] L. Beilina, M.V. Klibanov, and M.Yu Kokurin. Adaptivity with relaxation for ill-posed problems and global convergence for a coefficient inverse problem. *Journal of Mathematical Sciences*, 167(3):279–325, 2010.

[13] L. Beilina, K. Samuelsson, and K. Åhlander. Efficiency of a hybrid method for the wave equation. In *International Conference on Finite Element Methods*, Gakuto International Series Mathematical Sciences and Applications. Gakkotosho CO.,LTD, 2001.

[14] A. M. Bruckstein, B. C. Levy, and T. Kailath. Differential methods in inverse scattering. *SIAM J. Appl. Math.*, 45(2):312–335, 1985.

[15] M. Burger, S. Osher, and E. Yablonovitch. Inverse problem techniques for the design of photonic crystals. *IEICE Transactions on Electronics*, 87(C):258 – 265, 2004.

[16] M. Cheney and D. Isaacson. Inverse problems for a perturbed dissipative half-space. *Inverse Problems*, 11(4):865–888, 1995.

[17] Z. G. Dong, H. Liu, T. Li, Z. H. Zhu, S. M. Wang, J. X. Cao, S. N. Zhu, and X. Zhang. Optical loss compensation in a bulk left-handed metamaterial by the gain in quantum dots. *Appl. Phys. Lett.*, 96(4):044104, 2010.

[18] H. W. Engl, M. Hanke, and A. Neubauer. *Regularization of Inverse Problems*. Dordrecht, Kluwer, 1996.

[19] B. Engquist and A. Majda. Absorbing boundary conditions for the numerical simulation of waves. *Math. Comp.*, 31(139):629–651, 1977.

[20] A. Fang, Th. Koschny, M. Wegener, and C. M. Soukoulis. Self-consistent calculation of metamaterials with gain. *Phys. Rev. B*, 79:241104, 2009.

[21] J. W. Galusha, L. R. Richey, J. S. Gardner, J. N. Cha, and M. H. Bartl. Discovery of a diamond-based photonic crystal structure in beetle scales. *Phys. Rev. E*, 77(5):050904, 2008.

[22] D. J. Griffiths. *Introduction to Electrodynamics, Third Edition*. Prentice Hall, 1999.

[23] A. Håkansson, J. Sanchez-Dehesa, and L. Sanchis. Inverse design of photonic crystal devices. *IEEE Journal on selected areas in communications*, 23 (7):1365 – 1371, 2005.

[24] J. D. Joannopoulos, S. G. Johnson, J. N. Winn, and R. D. Meade. *Photonic Crystals: Molding the Flow of Light, 2nd ed.* Princton University Press, 2008.

[25] J. D. Joannopoulos, R. D. Meade, and J. N. Winn. *Photonic Crystals: Molding the Flow of Light*. Princeton University Press, 1995.

[26] S. John. Strong localization of photons in certain disordered dielectric superlattices. *Phys. Rev. Lett.*, 58(23):2486–2489, 1987.

[27] S. G. Johnson and J. D. Joannopoulos. *Introduction to Photonic Crystals: Bloch's Theorem, Band Diagrams, and Gaps (But No Defects)*. MIT, 2003.

[28] C. Y. Kao, S. Osher, and E. Yablonovitch. Maximizing band gaps in two-dimensional photonic crystals by using level set methods. *Applied Physics B: Lasers and Optics*, 81(2-3):235 – 244, 2005.

[29] T. A. Klar, A. V. Kildishev, V. P. Drachev, and V. M. Shalaev. Negative-index metamaterials: Going optical. *IEEE J. Sel. Top. Quantum Electron.*, 12(6):1106–1115, 2006.

[30] T. F. Krauss, R. M. De La Rue, and S. Brand. Two-dimensional photonic-bandgap structures operating at near-infrared wavelengths. *Nature*, 383:699–702, 1996.

[31] O. A. Ladyžhenskaya. *The boundary value problems of mathematical physics*. Springer-Verlag, New York, 1985.

[32] Ø. Lind-Johansen, K. Seip, and J. Skaar. The perfect lens on a finite bandwidth. *J. Math. Phys.*, 50(1):012908, 2009.

[33] J. Nocedal. Updating quasi-newton matrices with limited storage. *Math. Comp.*, 35(151):773–782, 1980.

[34] M. A. Noginov, G. Zhu, M. Bahoura, J. Adegoke, C. E. Small, B. A. Ritzo, V. P. Drachev, and V. M. Shalaev. Enhancement of surface plasmons in an Ag aggregate by optical gain in a dielectric medium. *Opt. Lett.*, 31(20):3022–3024, 2006.

[35] J. B. Pendry. Negative refraction makes a perfect lens. *Phys. Rev. Lett.*, 85(18):3966–3969, 2000.

[36] O. Pironneau. *Optimal shape design for elliptic systems*. Springer Verlag, Berlin, 1984.

[37] A. K. Popov and V. M. Shalaev. Compensating losses in negative-index metamaterials by optical parametric amplification. *Opt. Lett.*, 31(14):2169–2171, 2006.

[38] S. A. Ramakrishna and J. B. Pendry. Removal of absorption and increase in resolution in a near-field lens via optical gain. *Phys. Rev. B*, 67(20):201101, 2003.

[39] S. A. Ramakrishna, J. B. Pendry, D. Schurig, D. R. Smith, and S. Schultz. The asymmetric lossy near-perfect lens. *J. Mod. Optics*, 49(10):1747–1762, 2002.

[40] J. W. S. Rayleigh. On the remarkable phenomenon of crystalline reflexion described by Prof. Stokes. *Phil. Mag.*, 26:256–265, 1888.

[41] V. M. Shalaev. Optical negative-index metamaterials. *Nat. Photonics*, 1(1):41–48, 2007.

[42] Y. Sivan, S. Xiao, U. K. Chettiar, A. V. Kildishev, and V. M. Shalaev. Frequency-domain simulations of a negative-index material with embedded gain. *Opt. Express*, 17(26):24060–24074, 2009.

[43] J. Skaar. Negative refraction: A tutorial. `http://arxiv.org/abs/1008.3223`, 2010.

[44] J. Skaar, L. Wang, and T. Erdogan. On the synthesis of fiber bragg gratings by layer peeling. *IEEE Journal of Quantum Electronics*, 37(2):165–173, 2001.

[45] V. G. Veselago. The electrodynamics of substances with simultaneously negative values of ϵ and μ. *Sov. Phys. Usp.*, 10(4):509–514, 1968.

[46] M. A. Vincenti, D. de Ceglia, V. Rondinone, A. Ladisa, A. D'Orazio, M. J. Bloemer, and M. Scalora. Loss compensation in metal-dielectric structures in negative-refraction and super-resolving regimes. *Phys. Rev. A*, 80(5):053807, 2009.

[47] P. Vukusic and J. R. Sambles. Photonic structures in biology. *Nature*, 424:852–855, 2003.

[48] O. H. Waagaard and J. Skaar. Inverse scattering in multimode structures. *SIAM J. Appl. Math.*, 68(2):311–333, 2007.

[49] Wikipedia. Photonic crystals. `http://en.wikipedia.org/wiki/Photonic_crystal`, October 2011.

[50] Wikipedia. Well-posed probelm. `http://en.wikipedia.org/wiki/Well-posed_problem`, November 2011.

[51] E. Yablonovitch. Inhibited spontaneous emission in solid-state physics and electronics. *Phys. Rev. Lett.*, 58(20):2059–2062, 1987.

[52] E. Yablonovitch. Photonic crystals: What's in a name? *OPN*, pages 12–13, March 2007.

[53] E. Yablonovitch, T. J. Gmitter, and K. M. Leung. Photonic band structure: the face-centered-cubic case employing nonspherical atoms. *Phys. Rev. Lett.*, 67(17):2295–2298, 1991.

[54] A. E. Yalge and B. C. Levy. Layer-stripping solutions of multidimensional scattering problems. *Journal of Mathematical Physics*, 27(6):1701–1710, 1986.

[55] J. Zhang, H. Jiang, B. Gralak, S. Enoch, G. Tayeb, and M. Lequime. Compensation of loss to approach -1 effective index by gain in metal-dielectric stacks. *Eur. Phys. J. Appl. Phys.*, 46:32603, 2009.

Paper I

Effect of gain saturation in a gain compensated perfect lens

M. P. H. Andresen, A. V. Skaldebø, M. W. Haakestad, H. E. Krogstad and J. Skaar

Effect of gain saturation in a gain compensated perfect lens

Marte P. Hatlo Andresen,[1,*] **Aleksander V. Skaldebø,**[2,3] **Magnus W. Haakestad,**[4]
Harald E. Krogstad,[1] **and Johannes Skaar**[2,3]

[1]*Department of Mathematical Sciences, Norwegian University of Science and Technology,*
NO-7491 Trondheim, Norway
[2]*Department of Electronics and Telecommunications, Norwegian University of Science and Technology,*
NO-7491 Trondheim, Norway
[3]*University Graduate Center, NO-2027 Kjeller, Norway*
[4]*Norwegian Defence Research Establishment (FFI), P.O. Box 25, NO-2027 Kjeller, Norway*
*Corresponding author: hatlo@math.ntnu.no

The transmission of evanescent waves in a gain compensated perfect lens is discussed. In particular, the impact of gain saturation is included in the analysis, and a method for calculating the fields of such nonlinear systems is developed. Gain compensation clearly improves the resolution; however, a number of nonideal effects arise as a result of gain saturation. The resolution associated with the lens is strongly dependent on the saturation constant of the active medium. © 2010 Optical Society of America

OCIS codes: 260.2110, 160.4670, 160.3918.

1. INTRODUCTION

Metamaterials have large potential in electromagnetics and optics due to their possibility of tailoring the permittivity and permeability. This enables the construction of, for example, media with negative refractive indices n [1], perfect lenses [2], invisibility cloaks [3,4], and other exciting components transforming the electromagnetic field [5]. Unfortunately, the performance of such devices is strongly limited by losses. Although causality and passivity do not prohibit negative index materials with arbitrary low losses [6], in practice it is difficult to fabricate materials with high figure of merit (FOM) $=-\text{Re } n/\text{Im } n$, especially at optical frequencies [7–10]. For perfect lenses, losses limit the amplification of evanescent waves associated with large spatial frequencies, and therefore the resolution [11,12]. It has therefore been suggested to introduce gain into the metamaterials [7,13–21]. This could be a promising approach provided the intrinsic losses can be made relatively small so that compensation by a realistic amount of gain is possible.

Both permittivity ϵ and permeability μ may involve losses; thus, in general, gain may be needed to reduce *both* Im ϵ and Im μ. For a perfect lens it is generally not sufficient, e.g., to reduce Im ϵ below zero such that the refractive index $n=\sqrt{\epsilon\mu}$ becomes real. However, as long as the object to be imaged is one-dimensional, only one polarization [transverse electric or transverse magnetic (TM)] of the electromagnetic field is required. Then, provided the lens is sufficiently thin, only one of the parameters ϵ and μ is relevant for the transmission of evanescent waves [2,12]. Choosing TM polarization, only ϵ matters, enabling gain compensation with dielectric active media.

Introducing the necessary active material into a metamaterial leads to a change not only in the imaginary part but also in the real part of the permittivity, and should therefore be kept in mind while designing the metamaterial structure. Other critical considerations include matching of the negative refractive index frequency band to that of the gain line shape function, the level of loss possible to overcome in the absence of saturation, and the saturation constant of the active medium.

There have been several attempts to create a perfect lens in the near infrared (IR) spectrum for the last years [7–9,22]. The FOM currently reported is of the order of 3 for the frequency where Re $n \approx -1$ [8,9]. With these values, traditional optical amplifiers such as erbium-doped silica or gas laser amplifiers will not be able to reduce the intrinsic losses significantly. Theoretical studies have shown that it may be possible to raise the FOM at near IR frequencies to as much as 20, while keeping Re $n \approx -1$ [23]. It has also been reported that laser dyes, or dye-Ag aggregate mixtures, may reach amplifications of up to Im $n \approx -0.06$ at near IR frequencies [14,24]. Taking into account these reports, this article will not speculate further on the choice and design of the metamaterial, but merely assume that an appropriate material is physically feasible.

The main purpose of our work is to consider the transmission of evanescent waves in a practical gain compensated perfect lens. Clearly, gain saturation is highly relevant in this context, and we demonstrate how this effect leads to limited amplification of evanescent fields, and therefore limited resolution. We calculate the resolution as a function of the saturation constant of the active medium, and also the detailed field profile and reflections from the lens. It will become clear that gain saturation is a critical effect which may lead to severe limitations.

2. NONLINEAR GAIN SATURATION AND FIELD CALCULATIONS

The relative permittivity of the active metamaterial is given by

$$\epsilon(\omega) = 1 + \chi_p(\omega) + \chi_a(\omega), \tag{1}$$

where $\chi_p(\omega)$ denotes the susceptibility of the passive structure and $\chi_a(\omega)$ denotes the contribution from the active part. The contribution to the susceptibility for traveling and evanescent fields in active media can be modeled using semiclassical theory [25]. If there is spherical symmetry, allowing for coupling to several degenerate states with different values of the quantum number m, one can show using the Wigner–Eckart theorem and the general properties of the Clebsch–Gordan coefficients that the system can effectively be treated as a two-level system. Assuming two-level atoms and using the dipole approximation, we find the following expression for the active susceptibility:

$$\chi_a(\omega) = \frac{A(\omega)\left(\dfrac{\omega - \omega_0}{\gamma} - i\right)}{1 + \dfrac{|\mathbf{E}|^2}{\mathcal{E}_s(\omega)^2}}. \tag{2}$$

Here ω_0 is the transition frequency, ω is the frequency of the incident light, γ is a phenomenological decay rate due to spontaneous emission and elastic collisions, $\mathbf{E}$ is the complex electric field, and $\mathcal{E}_s(\omega)$ is the saturation constant of the active medium. The saturation constant depends on the selected gain material and pumping level. For dye amplifiers a normal value is $\mathcal{E}_s(\omega_0) \sim 10^7$ V/m [24,26], corresponding to intensities in the kW/cm^2 regime for propagating waves. The numerator in Eq. (2) describes the susceptibility in the limit $|\mathbf{E}|/\mathcal{E}_s \to 0$. The numerator contains the line shape function and several material parameters; factors that are irrelevant for the analysis below are absorbed into the function $A(\omega)$. For $\omega = \omega_0$ and $|\mathbf{E}|/\mathcal{E}_s \to 0$, $A(\omega)$ is simply $-\mathrm{Im}\,\chi_a(\omega)$. Both functions $A(\omega)$ and $\mathcal{E}_s(\omega)$ are real-valued. Note that the material parameters describing the active medium are effective parameters, depending on the geometry of the metamaterial structure, and are not necessarily equal to the bulk parameters of the gain material [18,19].

Throughout this paper, we will consider the frequency $\omega = \omega_0$. Equation (2) now reduces to

$$\chi_a(\omega_0) = \frac{-iA(\omega_0)}{1 + \dfrac{|\mathbf{E}|^2}{\mathcal{E}_s(\omega_0)^2}}. \tag{3}$$

Equation (3) describes how the imaginary part of the total permittivity relates to the pumping and local field amplitude. The real part of the total permittivity is independent of the pumping and local field.

Note that there is a fundamental difference between the nonlinearity due to gain saturation and conventional second- and third-order nonlinearities. First, the nonlinearity due to the denominator in Eq. (2) is so large that a Taylor expansion up to third order is generally not valid. Second, the nonlinearity of a gain medium is expressed in

terms of the slowly varying field envelope $|\mathbf{E}|$, while the second- and third-order nonlinearities usually are expressed in terms of the rapidly varying time-dependent electric field. Since the nonlinearity in our case can be characterized using $|\mathbf{E}|$, the medium will not generate new frequencies for monochromatic input [27]. Nevertheless, if several modes (or frequencies) are present, the modes interact in the sense that the complex refractive index seen by one mode is dependent on the presence and strength of all modes.

We consider a perfect lens slab which extends to infinity in the xy-plane and has thickness d in the z-direction (see Fig. 1). The source is located a distance a (with $a < d$) from the input end of the lens. The incident field from the source will be taken to be a superposition of plane TM waves, with the magnetic field in the y-direction. Provided $\omega_0 d/c \ll 1$ and $|\mu| \sim 1$, the specific value of μ is not critical for the operation of the lens for evanescent waves [2,12]. Here c is the vacuum light velocity. The permittivity is given by Eqs. (1) and (3), and Re $\chi_p(\omega_0) = -2$. The remaining losses after gain compensation (in the absence of saturation) is described by the parameter

$$\Delta\chi = \mathrm{Im}\,\chi_p(\omega_0) - A(\omega_0). \tag{4}$$

To find the steady state solution to Maxwell's equations for our nonlinear medium, an iterative approach can be used. In the zeroth iteration, the electric field is simply set to zero everywhere. (Alternatively, the initial field could be set to infinity. This does not give any significant difference in the performance, in terms of the required number of iterations.) In the next iteration, Eqs. (1) and (3) are used to find an approximation of the permittivity of the lens. Taking the incident magnetic field to be unity (normalized), we can compute the magnetic and electric fields everywhere. Now we may repeat the iteration; calculate a new approximation of the permittivity from the field, compute the resulting field from this new structure, etc. The iteration procedure has an inherent stability, as growing fields lead to less gain in the medium, and vice versa.
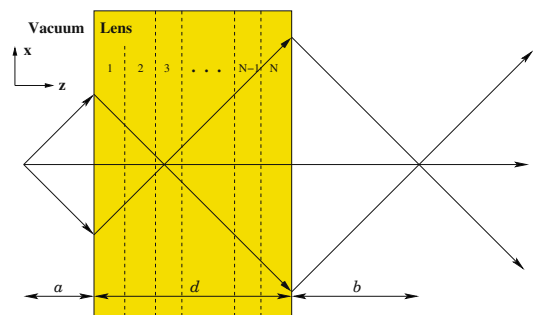

Fig. 1. (Color online) Perfect lens in vacuum. The parameter d is the thickness of the lens, and a and b are the distances from the source to the lens, and from the lens to the image plane, respectively. The parameters are governed by the equation $d = a + b$. The numbers 1 through N indicate the different slices. The lens is considered to be infinite in the xy-plane.

Nevertheless, inaccuracies and even divergence may arise if the number of slices is too low so that the field no longer can be treated as a constant in each slice. In the case $\Delta\chi=0$ the convergence seems to be particularly sensitive to the number of slices. An alternative to increasing the number of slices to a very high number is to regularize the iterative approach as follows: Rather than setting the permittivity to that resulting from the field in the previous iteration, it can be set to a weighted mean of the permittivities as resulting from the last two iterations. In our computations, the permittivity in the iteration i (for $i \geq 2$) was set to 0.5 times the permittivity calculated by the field from iteration $i-1$, plus 0.5 times that resulting from iteration $i-2$. For $i=1$ the permittivity was calculated using the field from iteration 0. This resulted in convergence after ~20–35 iterations. The weight factor of 0.5 is somewhat arbitrary; other choices are possible but may require a larger N or number of iterations to obtain convergence.

If the root mean square deviation of three successive iterations is within a specified limit (10^{-12} for the relative permittivity in our computations), and strictly decreasing, the results are deemed converged. Note that when the fields of subsequent iterations coincide, we have a valid solution to Maxwell's equations with constitute relation as implied by Eqs. (1) and (3).

In general, the fields in one iteration, and therefore the permittivity in the next iteration, will be dependent on x and z. Thus the computation of the fields in the next iteration requires the solution to Maxwell's equations in an inhomogeneous structure. Note that, in each iteration, the structure is linear; the nonlinearity of the structure enters through the iteration. For the linear calculation, we employ a transfer matrix technique, considering the different plane waves in the structure. The lens is divided into N slices in the xy-plane as seen in Fig. 1. These slices must be sufficiently thin, such that the permittivity inside each slice is approximately uniform in the z-direction. For this condition to be valid for the next iteration as well, the resulting field from the present iteration must also be approximately constant. This means that $k_x d/N \lesssim 1$ for the transverse wavenumbers k_x that contribute significantly to the fields.

The electric field can be found using the Ampere–Maxwell's law,

$$\mathbf{E}(x,z) = \frac{1}{-i\omega\epsilon(x,z)\epsilon_0} \nabla \times \mathbf{H}(x,z). \tag{5}$$

With periodic boundary conditions in the x-direction, the magnetic field and the permittivity can be expanded in discrete Fourier series,

$$\mathbf{H}(x,z) = H(x,z)\hat{\mathbf{y}} = \sum_m h_m(z)\exp(ik_{xm}x)\hat{\mathbf{y}}, \tag{6}$$

$$\epsilon(x,z) = \sum_m e_m(z)\exp(ik_{xm}x), \tag{7}$$

for some Fourier coefficients $h_m(z)$ and $e_m(z)$. Here $k_{xm} = 2\pi m/L$, L is the computational domain, and $\hat{\mathbf{y}}$ is the unit vector in the y-direction.

From Maxwell's equations, we find that the magnetic field satisfies

$$\nabla^2 H + \epsilon\mu k^2 H - \frac{1}{\epsilon}\frac{\partial\epsilon}{\partial x}\frac{\partial H}{\partial x} = 0, \tag{8}$$

where $k = \omega_0/c$. We express $1/\epsilon$ and $(1/\epsilon)\partial\epsilon/\partial x$ as Fourier series as follows:

$$\frac{1}{\epsilon(x)} = \sum_m Q_m \exp(ik_{xm}x), \tag{9}$$

$$\frac{1}{\epsilon(x)}\frac{\partial\epsilon(x)}{\partial x} = \sum_m F_m \exp(ik_{xm}x). \tag{10}$$

The Fourier coefficients F_m are now given as

$$F_m = \sum_{m'} Q_{m-m'}ik_{xm'}e_{m'}, \tag{11}$$

or as a matrix product

$$F = i\mathbf{Q}\mathbf{k_x}\mathbf{e}, \tag{12}$$

where $F = \{F_m\}_m$, $\mathbf{k_x} = \mathrm{diag}(k_{xm})$, $\mathbf{e} = \{e_m\}_m$, and $\mathbf{Q}$ is a Toeplitz matrix with elements $\mathbf{Q}_{i,j} = Q_{i-j}$.

Inserting the Fourier series into Eq. (8), we obtain

$$\frac{d^2 h_m(z)}{dz^2} - k_{xm}^2 h_m(z) + k^2\mu\sum_{m'}\varepsilon_{m-m'}(z)h_{m'}(z)$$

$$- \sum_{m'} iF_{m-m'}k_{xm'}h_{m'} = 0, \tag{13}$$

for each m. Let $\mathbf{h} = \{h_m\}_{m\in\mathbb{Z}}$ and use $k_{zm}^2 = k^2 - k_{xm}^2$. We can write Eq. (13) as a matrix equation,

$$\frac{d^2\mathbf{h}(z)}{dz^2} + [\mathbf{k_z}^2 + \mathbf{V}]\mathbf{h}(z) = 0, \tag{14}$$

where $\mathbf{k_z} = \mathrm{diag}(k_{zm})$, and $\mathbf{V}$ is the operator defined as

$$\mathbf{V} = -k^2\mathbf{I} + k^2\mu\mathbf{G} - \mathbf{F}. \tag{15}$$

Here $\mathbf{G}$ and $\mathbf{F}$ are infinite dimensional Toeplitz matrices with elements $\mathbf{G}_{i,j} = e_{i-j}$ and $\mathbf{F}_{i,j} = iF_{i-j}k_{xj}$.

Equation (14) may be decomposed into a first-order system by writing $\mathbf{h} = \mathbf{h}^+ + \mathbf{h}^-$, where $\mathbf{h}^+ = \{h_m^+\}_{m\in\mathbb{Z}}$ and $\mathbf{h}^- = \{h_m^-\}_{m\in\mathbb{Z}}$. In fact, the equations

$$\frac{d\mathbf{h}^+}{dz} = i\mathbf{k_z}\mathbf{h}^+ + i(2\mathbf{k_z})^{-1}\mathbf{V}(\mathbf{h}^+ + \mathbf{h}^-), \tag{16a}$$

$$\frac{d\mathbf{h}^-}{dz} = -i\mathbf{k_z}\mathbf{h}^- - i(2\mathbf{k_z})^{-1}\mathbf{V}(\mathbf{h}^+ + \mathbf{h}^-), \tag{16b}$$

are seen to be equivalent to Eq. (14) after differentiation and summation. This decomposition is particularly convenient since outside the lens $\mathbf{V}=0$, and Eqs. (16) have the simple solution $h_m^\pm(z) = \mathrm{const}\cdot\exp(\pm ik_{zm}z)$. In other words, outside the lens, h_m^+ and h_m^- are the forward and backward propagating waves, respectively.

By adding Eqs. (16a) and (16b), we obtain

$$\frac{d\mathbf{h}}{dz} = i\mathbf{k_z}(\mathbf{h}^+ - \mathbf{h}^-), \tag{17}$$

which is needed for $\nabla \times \mathbf{H}$. By writing

$$\Psi = \begin{bmatrix} \mathbf{h}^+ \\ \mathbf{h}^- \end{bmatrix}, \quad \mathbf{C} = \begin{bmatrix} i\mathbf{k_z} + i(2\mathbf{k_z})^{-1}\mathbf{V} & i(2\mathbf{k_z})^{-1}\mathbf{V} \\ -i(2\mathbf{k_z})^{-1}\mathbf{V} & -i\mathbf{k_z} - i(2\mathbf{k_z})^{-1}\mathbf{V} \end{bmatrix}, \tag{18}$$

Eqs. (16) may be brought into matrix form,

$$\frac{d\Psi}{dz} = \mathbf{C}\Psi. \tag{19}$$

Since the permittivity is assumed to be independent of z within a slice of the lens, the matrix $\mathbf{C}$ will be constant for each slice. Thus, Eq. (19) can be integrated to obtain

$$\Psi(z_b) = \exp\{(z_b - z_a)\mathbf{C}\}\Psi(z_a), \tag{20}$$

for z_a and z_b inside the same slice. Let z_j be at the left hand side of slice j, Δ_j be the thickness of the slice, and $\mathbf{C}_j$ be the $\mathbf{C}$-matrix for layer j. From the field at z_j, we find the field at the right hand side of the slice as

$$\Psi(z_j + \Delta_j) = \exp\{\Delta_j\mathbf{C}_j\}\Psi(z_j). \tag{21}$$

Note that $j=0$ corresponds to the region between the source and the lens, $j=1, \ldots, N$ are the slices inside the lens, and $j=N+1$ represents the region from the lens to the image plane. The thicknesses are $\Delta_0 = a$, $\Delta_j = d/N$, for $j=1, \ldots, N$, and $\Delta_{N+1} = b$. Let us define

$$\mathcal{M}_j = \exp\{\Delta_j\mathbf{C}_j\}. \tag{22}$$

Equation (22) propagates the field from the start of a slice to the end. Next, connecting the fields of adjacent slices with the electromagnetic boundary conditions, we find for the boundary between slice j and $j+1$ that

$$\frac{\partial H_{j+1}(z_{j+1})}{\partial z} = \frac{\epsilon_{j+1}}{\epsilon_j}\frac{\partial H_j(z_{j+1})}{\partial z}. \tag{23}$$

Inserting the Fourier series from Eqs. (6) and (7), we obtain a convolution on the right hand side corresponding to the multiplication of a Toeplitz matrix and the vector containing the components $dh_m(z)/dz$. The Toeplitz matrix is defined by the Fourier components of $\epsilon_{j+1}/\epsilon_j$ and will be called $\mathbf{P}$. Then

$$\frac{d\mathbf{h}_j}{dz}(z_{j+1}) = \mathbf{P}_j(z_{j+1})\frac{d\mathbf{h}_{j+1}}{dz}(z_{j+1}), \tag{24}$$

where $\mathbf{P}_j$ corresponds to the transition between layers j and $j+1$.

Equation (24) together with the fact that $\mathbf{h}$ is continuous across the layer boundary gives us the following transfer matrix:

$$\begin{bmatrix} \mathbf{h}_{j+1}^+ \\ \mathbf{h}_{j+1}^- \end{bmatrix} = \frac{1}{2}\begin{bmatrix} \mathbf{I} + \mathbf{k_z}^{-1}\mathbf{P}_j\mathbf{k_z} & \mathbf{I} - \mathbf{k_z}^{-1}\mathbf{P}_j\mathbf{k_z} \\ \mathbf{I} - \mathbf{k_z}^{-1}\mathbf{P}_j\mathbf{k_z} & \mathbf{I} + \mathbf{k_z}^{-1}\mathbf{P}_j\mathbf{k_z} \end{bmatrix}\begin{bmatrix} \mathbf{h}_j^+ \\ \mathbf{h}_j^- \end{bmatrix}. \tag{25}$$

Let us call the transfer matrix in Eq. (25) $\mathcal{P}_j$.

By the successive application of Eqs. (22) and (25), we find

$$\begin{bmatrix} \mathbf{T} \\ \mathbf{0} \end{bmatrix} = \mathcal{M}_{N+1}\prod_{j=N}^{0}(\mathcal{P}_j\mathcal{M}_j)\begin{bmatrix} \mathbf{I} \\ \mathbf{R} \end{bmatrix}. \tag{26}$$

Here, each column i of $\mathbf{I}$ corresponds to an experiment where the incident field amplitude is 1 for one of the Fourier components and zero for the others. The ith column of $\mathbf{R}$ is the reflection at the source plane of experiment i, and the ith column of $\mathbf{T}$ is the corresponding transmission at the image plane. To get the reflection in the case of two or more waves, the corresponding columns of $\mathbf{R}$ are added; the new transmission is found by adding columns of $\mathbf{T}$. Once the total matrix in Eq. (26) has been found, it is straightforward to calculate the unknowns $\mathbf{T}$ and $\mathbf{R}$, and therefore the field amplitudes in all slices.

3. NUMERICAL RESULTS

The thickness d of the lens was chosen such that $\omega_0 d/c = 2\pi/10$. The resolution clearly improves with decreasing distance b from the lens to the image, since then the required evanescent fields at the end of the lens are reduced. However there may be practical reasons that make it impossible to reduce the distances a and b below a certain value. In our simulations we have taken $a=b=d/2$. For simplicity we normalized $\epsilon_0 = \mu_0 = \omega_0 = 1$. The permeability was set to $\mu = -1$; however, since the lens was relatively thin, the specific value of μ did not matter significantly for evanescent TM waves. The number of slices was taken to be $N=20$. The computation domain L was chosen in the range (15,50) depending on the specific problem, and the number of Fourier components (m values) was of the order of 100.

First, a single mode source $\mathbf{H} = \exp(ik_x x + ik_z z)\hat{\mathbf{y}}$ was considered. The reflection and transmission coefficients, and the fields in the lens, were computed using the iterative method above. The transmission coefficient is shown in Fig. 2. It is easy to see improvements as a result of gain compensation, dependent on the saturation constant $\mathcal{E}_s$.
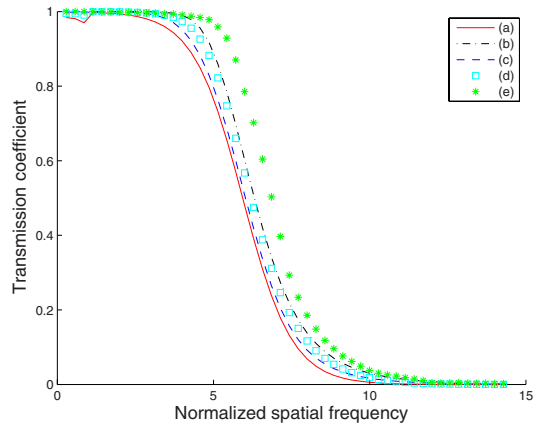

Fig. 2. (Color online) The absolute value of the transmission coefficient when $\omega_0/c = 1$ (normalized), $\omega_0 d/c = 2\pi/10$, $a=b=d/2$, Im $\chi_p(\omega_0) = 0.05$, and $N=20$: (a) Noncompensated lens; (b) $\mathcal{E}_s = 10$, $\Delta\chi = 0$; (c) $\mathcal{E}_s = 4$, $\Delta\chi = 0$; (d) $\mathcal{E}_s = 10$, $\Delta\chi = 0.015$; (e) $\mathcal{E}_s = 10$, $\Delta\chi = 0$, two waves, k_x and $-k_x$, both having amplitude of 1/2.

(Here it is useful to recall that for a normalized magnetic field $\mathbf{H}=\exp(ik_x x+ik_z z)\hat{\mathbf{y}}$, the electric field is $\mathbf{E}=([k_z/\omega_0\epsilon\epsilon_0]\hat{\mathbf{x}}-[k_x/\omega_0\epsilon\epsilon_0]\hat{\mathbf{z}})\exp(ik_x x+ik_z z)$. Thus, for our normalization, we see that $|\mathbf{E}|\sim k_x$, to be compared to $\mathcal{E}_s$.) Nevertheless, for a fixed amplitude of the incident field, Fig. 3 indicates that an exponential increase in the saturation constant is needed for a linear increase in the resolution. This is an important result as it shows the difficulty of getting large resolution: The required large evanescent fields associated with large spatial frequencies saturate the gain at the output of the lens.

The reflection coefficient is plotted in Fig. 4. We note that significant reflections arise even for the spatial frequencies where the transmission is relatively large. As can be seen in Fig. 5, the field distributions of the two evanescent components in the lens increase roughly exponentially with $+z$ or $-z$, respectively. For small spatial frequencies, where the lens is essentially perfect, the one increasing in the $+z$-direction dominates. For higher spatial frequencies the two components have a similar amplitude, such that the total field and therefore the imaginary part of the permittivity start to look like a U-shaped valley.

In general, different plane wave components of the source will couple to each other through Eq. (3). To simulate the gain compensated lens under more real-world conditions, it was therefore tested with several waves traversing the lens simultaneously. The transmission of one wave as a function of k_x, in the presence of another wave $-k_x$, is shown in Fig. 2. The amplitudes of both waves were set to 1/2 to keep the total field at the source equal to the case with a single wave. Moreover, from a number of simulations with several waves, a useful rule of thumb was discovered: As a worst-case estimate, one can judge whether the lens operates as required by assuming that the mode with largest k_x has amplitude equal to the sum of the amplitudes at the source. More precisely, suppose that a single mode k_x with an amplitude of 1 experiences a transmission greater than 1/2. For any superposition of

modes with transversal wavenumbers less than k_x and sum of amplitudes equal to unity, each mode will experience a transmission greater than 1/2.

For conventional lenses, the Rayleigh criterion is usually applied to quantify the distance between two point sources (or, in the one-dimensional case, line sources) in order to resolve their images. Since our lens is nonlinear, the image of two line sources cannot be determined as a superposition of the fields associated with the two sources separately or as a superposition of the fields associated with their Fourier components. Therefore, as in previous literature on perfect lenses, we have chosen to consider a single Fourier component source and defined the spatial resolution as $2\pi/k_x$, where k_x is the half-maximum wave-

Fig. 4. (Color online) The absolute value of the reflection coefficient at the source plane after convergence, for the same cases as those in Fig. 2.
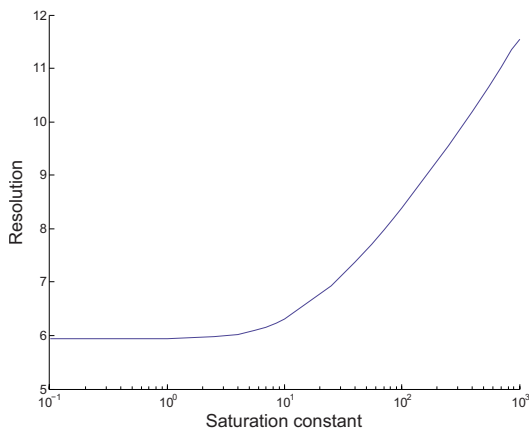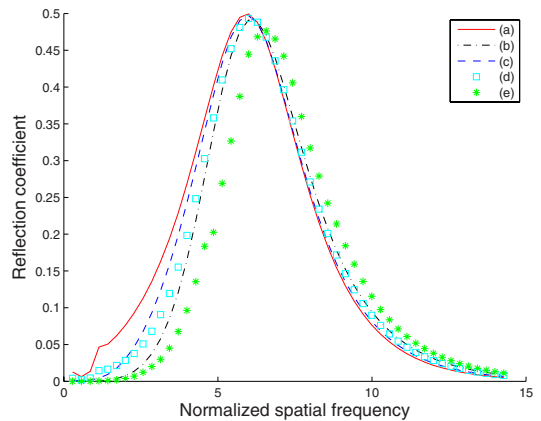

Fig. 3. (Color online) The resolution of the lens as a function of the saturation constant. The resolution is defined as the k_x-value where the transmission equals 1/2. Parameters: $\omega_0/c=1$, $\omega_0 d/c=2\pi/10$, Im $\chi_p(\omega_0)=0.05$, $\Delta\chi=0$, $a=b=d/2$, and $N=20$.
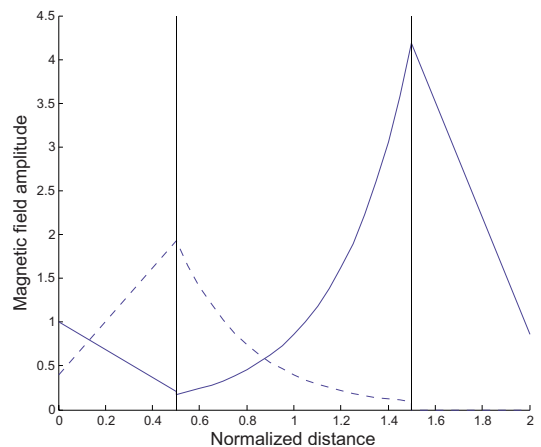

Fig. 5. (Color online) The distribution of the two components of the evanescent field in the lens, for one wave with $k_x=5.1408$. The distance is normalized with respect to lens thickness d. Parameters: $\omega_0/c=1$, $\omega_0 d/c=2\pi/10$, Im $\chi_p(\omega_0)=0.05$, $\Delta\chi=0$, $\mathcal{E}_s=10$, $a=b=d/2$, and $N=20$. The solid line shows the absolute value of the nonzero component of $\mathbf{h}^+$, and the dotted line shows the absolute value of the nonzero component of $\mathbf{h}^-$.

number (Fig. 3). Note that the behavior of the lens for more complex sources can be determined from the rule of thumb described above.

Figure 6 shows the absolute value of the transmitted magnetic field at the image plane, $|H(x, 2d)|$, resulting from a source consisting of two slits. The image of the slits are clearly better resolved with an increased saturation constant $\mathcal{E}_s$.

4. CONCLUSION

We have developed a method for calculating the transmission, reflection, and detailed field profile of a gain compensated perfect lens, taking into account gain saturation. The gain compensation clearly improves the resolution limit of perfect lenses. However, due to gain saturation, a number of nonideal effects arise, including limited resolution and reflections. The nonideal effects depend heavily on the saturation constant and/or the field strength of the source.

If there are different waves traversing the lens at the same time, they will interact through the material. Waves with a spatial frequency close to the resolution limit will have the greatest impact. As a rule of thumb, it is enough to know the sum of amplitudes of the waves at the source, and then assume that the mode with the largest spatial frequency has this amplitude. If this single wave is transmitted, in the sense of a transmission larger than 1/2, then so will any superposition of waves with less spatial frequencies and the same sum of amplitudes.

The calculations in this work were performed for TM polarization and a one-dimensional source. For a two-dimensional source with both polarizations, both dielectric and magnetic losses should be compensated, that is, Im ϵ and Im μ must be reduced. Although the theory in this paper can trivially be extended to this situation, there may be serious practical problems associated with the fabrication of such active media for optical frequencies.

For a noncompensated lens, the maximum spatial frequency resolved by the lens is approximately $-(1/d)\ln(|1 + \epsilon|/2)$ [11,12]. Thus, for a fixed d, an exponential decrease in the losses is necessary to increase the resolution linearly. From our numerical results, a similar relation is approximately valid for the saturation constant of a gain compensated medium; to achieve a linear improvement in the resolution, the saturation constant must increase exponentially. This clearly shows the difficulties of achieving very high resolutions.

REFERENCES

1. V. G. Veselago, "The electrodynamics of substances with simultaneously negative ϵ and μ," Sov. Phys. Usp. **10**, 509–514 (1968).
2. J. B. Pendry, "Negative refraction makes a perfect lens," Phys. Rev. Lett. **85**, 3966–3969 (2000).
3. J. B. Pendry, D. Schurig, and D. R. Smith, "Controlling electromagnetic fields," Science **312**, 1780–1782 (2006).
4. U. Leonhardt, "Optical conformal mapping," Science **312**, 1777–1780 (2006).
5. U. Leonhardt and T. G. Philbin, "General relativity in electrical engineering," New J. Phys. **8**, paper 247 (2006).
6. B. Nistad and J. Skaar, "Causality and electromagnetic properties of active media," Phys. Rev. E **78**, 036603 (2008).
7. V. M. Shalaev, "Optical negative-index metamaterials," Nat. Photonics **1**, 41–48 (2007).
8. V. M. Shalaev, W. Cai, U. K. Chettiar, H. K. Yuan, A. K. Sarychev, V. P. Drachev, and A. V. Kildishev, "Negative index of refraction in optical metamaterials," Opt. Lett. **30**, 3356–3358 (2005).
9. G. Dolling, C. Enkrich, M. Wegener, C. M. Soukoulis, and S. Linden, "Low-loss negative-index metamaterials at telecommunication wavelengths," Opt. Lett. **31**, 1800–1802 (2006).
10. D. H. Kwon, D. H. Werner, A. V. Kildishev, and V. M. Shalaev, "Dual-band negative-index metamaterials in the near-infrared frequency range," in *Proceedings of IEEE Antennas and Propagation Society International Symposium* (IEEE, 2007), pp. 2861–2864.
11. S. Anantha Ramakrishna, J. B. Pendry, D. Schurig, D. R. Smith, and S. Schultz, "The asymmetric lossy near-perfect lens," J. Mod. Opt. **49**, 1747–1762 (2002).
12. Ø. Lind-Johansen, K. Seip, and J. Skaar, "The perfect lens on a finite bandwidth," J. Math. Phys. **50**, 012908 (2009).
13. S. Anantha Ramakrishna and J. B. Pendry, "Removal of absorption and increase in resolution in a near-field lens via optical gain," Phys. Rev. B **67**, 201101 (2003).
14. M. A. Noginov, G. Zhu, M. Bahoura, J. Adegoke, C. E. Small, B. A. Ritzo, V. P. Drachev, and V. M. Shalaev, "Enhancement of surface plasmons in an Ag aggregate by optical gain in a dielectric medium," Opt. Lett. **31**, 3022–3024 (2006).
15. A. K. Popov and V. M. Shalaev, "Compensating losses in negative-index metamaterials by optical parametric amplification," Opt. Lett. **31**, 2169–2171 (2006).
16. T. A. Klar, A. V. Kildishev, V. P. Drachev, and V. M. Shalaev, "Negative-index metamaterials: Going optical," IEEE J. Sel. Top. Quantum Electron. **12**, 1106–1115 (2006).
17. J. Zhang, H. Jiang, B. Gralak, S. Enoch, G. Tayeb, and M. Lequime, "Compensation of loss to approach -1 effective index by gain in metal-dielectric stacks," Eur. Phys. J.: Appl. Phys. **46**, 32603–32608 (2009).
18. A. Fang, Th. Koschny, M. Wegener, and C. M. Soukoulis, "Self-consistent calculation of metamaterials with gain," Phys. Rev. B **79**, 241104 (2009).
19. Y. Sivan, S. Xiao, U. K. Chettiar, A. V. Kildishev, and V. M. Shalaev, "Frequency-domain simulations of a negative-index material with embedded gain," Opt. Express **17**, 24060–24074 (2009).
20. M. A. Vincenti, D. de Ceglia, V. Rondinone, A. Ladisa, A. D'Orazio, M. J. Bloemer, and M. Scalora, "Loss compensa-
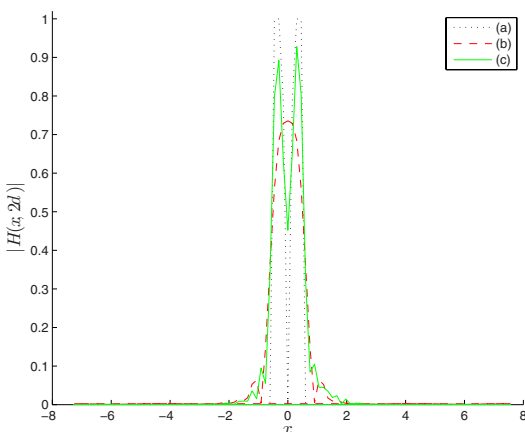
Fig. 6. (Color online) The absolute value of the transmitted magnetic field at the image plane, when the source consists of two slits. Parameters: $\omega_0/c = 1$, $\omega_0 d/c = 2\pi/10$, Im $\chi_p(\omega_0) = 0.05$, $\Delta\chi = 0$, $a = b = d/2$, and $N = 20$: (a) The incident magnetic field at the source, (b) $\mathcal{E}_s = 0.1$, and (c) $\mathcal{E}_s = 50$.

tion in metal-dielectric structures in negative-refraction and super-resolving regimes," Phys. Rev. A **80**, 053807 (2009).

21. Z. G. Dong, H. Liu, T. Li, Z. H. Zhu, S. M. Wang, J. X. Cao, S. N. Zhu, and X. Zhang, "Optical loss compensation in a bulk left-handed metamaterial by the gain in quantum dots," Appl. Phys. Lett. **96**, 044104 (2010).

22. C. Enkrich, M. Wegener, S. Linden, S. Burger, L. Zschiedrich, F. Schmidt, J. F. Zhou, Th. Koschny, and C. M. Soukoulis, "Magnetic metamaterials at telecommunication and visible frequencies," Phys. Rev. Lett. **95**, 203901 (2005).

23. S. Zhang, W. Fan, N. C. Panoiu, K. J. Malloy, R. M. Osgood, and S. R. J. Brueck, "Optical negative-index bulk metamaterials consisting of 2D perforated metal-dielectric stacks," Opt. Express **14**, 6778–6786 (2006).

24. N. M. Lawandy, "Localized surface plasmon singularities in amplifying media," Appl. Phys. Lett. **85**, 5040–5042 (2004).

25. M. O. Scully and M. S. Zubairy, "Atom-field interaction—semiclassical theory," in *Quantum Optics* (Cambridge Univ. Press, 1997), pp. 145–192.

26. M. G. Destro and M. S. Zubairy, "Small-signal gain and saturation intensity in dye laser amplifiers," Appl. Opt. **31**, 7007–7011 (1992).

27. O. Svelto, *Principles of Lasers* (Plenum, 1998).

Paper II

Inverse scattering of two-dimensional photonic structures by layer stripping

M. P. H.Andresen, H. E. Krogstad and J. Skaar

Inverse scattering of two-dimensional photonic structures by layer stripping

Marte P. Hatlo Andresen,[1] Harald E. Krogstad,[1] and Johannes Skaar[2,3,*]

[1]*Department of Mathematical Sciences, Norwegian University of Science and Technology, NO-7491 Trondheim, Norway*
[2]*Department of Electronics and Telecommunications, Norwegian University of Science and Technology,*
NO-7491 Trondheim, Norway
[3]*University Graduate Center, NO-2027 Kjeller, Norway*
*Corresponding author: johannes.skaar@iet.ntnu.no

Design and reconstruction of two-dimensional (2D) and three-dimensional photonic structures are usually carried out by forward simulations combined with optimization or intuition. Reconstruction by means of layer stripping has been applied in seismic processing as well as in design and characterization of one-dimensional photonic structures such as fiber Bragg gratings. Layer stripping is based on causality, where the earliest scattered light is used to recover the structure layer by layer. Our setup is a 2D layered nonmagnetic structure probed by plane-polarized harmonic waves entering normal to the layers. It is assumed that the dielectric permittivity in each layer only varies orthogonal to the polarization. Based on obtained reflectance data covering a suitable frequency interval, time-localized pulse data are synthesized and applied to reconstruct the refractive index profile in the leftmost layer by identifying the local, time-domain Fresnel reflection at each point. Once the first layer is known, its impact on the reflectance data is stripped off and the procedure repeated for the next layer. Through numerical simulations it will be demonstrated that it is possible to reconstruct structures consisting of several layers. The impact of evanescent modes and limited bandwidth is discussed.   © 2011 Optical Society of America

OCIS codes: 050.5298, 290.3200.

1. INTRODUCTION

Photonic crystals have been an exciting field of research since Yablonovitch and John published their papers in 1987 [1,2]. Photonic crystals are periodic structures designed to affect the propagation of electromagnetic waves [3]. The usual way of constructing such optical components is to carry out numerical simulations of electromagnetic waves hitting and being scattered off a trial design. The design is then changed by optimization or intuition until the structure has the desired properties. In this paper we use a layer-stripping procedure to show that it is possible to reconstruct a photonic structure from a set of reflectance data based on harmonic waves. In other words, we will look at how the inverse problem can be solved. The ultimate goal is to be able to reconstruct the structures from the observations and use this as a supplementary tool for the design of structures with desired features.

The idea of layer stripping is to reconstruct the properties of a medium from scattered data originating from an emitted wave pulse on the boundary of the domain. Layer stripping is based on causality, where the earliest scattered wave from each depth layer is used to recover the structure layer by layer. The method was first used in solving inverse acoustic scattering problems for seismic data; overviews can be found in [4,5]. Later, the method has also been applied to the design and characterization of one-dimensional photonic crystal structures such as fiber Bragg gratings [6] and multimode structures [7].

In the present simulation study, we are considering a two-dimensional (2D) structure, layered normal to the z direction, with periodically varying refractive index in the x direction while being constant in the y direction. The structure is probed by plane-polarized harmonic electromagnetic waves traveling in the z direction, with the electric field vector pointing in the y direction, thus representing a 2D wave propagation problem.

The forward problem, consisting of obtaining reflectance data for a known structure, may be formulated in terms of transfer matrices, providing reflection and transmission matrices for each layer as well as the whole structure. The corresponding inverse problem, consisting of recovering the properties of the unknown structure from the reflectance data, requires data for several wavenumbers and a range of frequencies.

The key step of the synthetic layer-stripping algorithm is to combine reflectance data for different frequencies so as to synthesize data from a short pulse at the time the pulse hits the surface. The data may then be applied to reconstruct the refractive index profile in the leftmost layer by identifying the local, time-domain Fresnel reflection at each point. Once the first layer is known, its transfer matrix may be computed and the impact of the layer on the reflectance data eliminated. The same idea is then applied to the modified reflectance data, and continuing in the same way, we are, at least in principle, able to reconstruct the whole structure.

2. FORWARD PROBLEM

We are considering photonic crystals consisting of homogeneous, dielectric, and nonmagnetic ($\mu = \mu_0$) materials, where the dielectric permittivity, $\epsilon(x,z)$, is varying in the x and z directions and constant in the y direction. The structure consists of layers orthogonal to the z axis, with ϵ constant with

respect to z (and y) in each layer. We assume that the structure contains N layers of finite thickness occupying the space from $z_0 = 0$ to z_N. Layer i spans $z_{i-1} \le z \le z_i$, with a thickness $\Delta_i = z_i - z_{i-1}$, and permittivity $\epsilon_i(x)$. Outside the structure we assume that it is vacuum. By inserting the Fourier transform in time of the electric and magnetic fields, e.g.,

$$\mathbf{E}(\mathbf{x}, t) = \frac{1}{2\pi} \int_{-\infty}^{\infty} \mathbf{e}(x, z, \omega) e^{-i\omega t} \mathrm{d}\omega, \qquad (1)$$

and similarly for $\mathbf{H}$ into Maxwell's equations, we obtain

$$\nabla \times \mathbf{e}(x, z, \omega) - i\omega\mu_0 \mathbf{h}(x, z, \omega) = 0, \qquad (2)$$

$$\nabla \times \mathbf{h}(x, z, \omega) + i\omega\epsilon_0 \epsilon(x, z)\mathbf{e}(x, z, \omega) = 0, \qquad (3)$$

$$\nabla \cdot (\epsilon(x, z)\mathbf{e}(x, z, \omega)) = 0, \qquad (4)$$

$$\nabla \cdot \mathbf{h}(x, z, \omega) = 0. \qquad (5)$$

In addition, from the standard continuity conditions for $\mathbf{E}$ and $\mathbf{H}$, parallel ($\parallel$) and orthogonal ($\perp$) to the layer boundaries, the following conditions have to apply:

$$\epsilon_1 \mathbf{e}_1^\perp = \epsilon_2 \mathbf{e}_2^\perp, \qquad (6)$$

$$\mathbf{e}_1^\parallel = \mathbf{e}_2^\parallel, \qquad (7)$$

$$\mathbf{h}_1 = \mathbf{h}_2. \qquad (8)$$

Omitting the dependence of ω, direct substitution shows that the Fourier transformed Maxwell's equations in the present case admit solutions of the form

$$\mathbf{e}(x, z) = e(x, z)\hat{\mathbf{y}}, \qquad (9)$$

$$\mathbf{h}(x, z) = \frac{1}{i\omega\mu_0} \left(-\frac{\partial e(x, z)}{\partial z}\hat{\mathbf{x}} + \frac{\partial e(x, z)}{\partial x}\hat{\mathbf{z}} \right), \qquad (10)$$

provided $e(x, z)$ satisfies the scalar Helmholtz equation,

$$\frac{\partial^2 e}{\partial x^2} + \frac{\partial^2 e}{\partial z^2} + \epsilon(x, z)k^2 e = 0, \qquad (11)$$

where $k = \omega/c_0$, $c_0^2 = 1/\mu_0\epsilon_0$, and e as well as its partial derivatives are continuous across the layer boundaries.

The structure will be probed using the plane-polarized waves in Eqs. (9) and (10), and all transmitted and reflected waves will have the same polarization.

The direct problem consists in solving Eq. (11) with appropriate boundary conditions. These will be plane waves entering from the half-space $z \le 0$ (thus, having positive z component wavenumbers), whereas no waves are supposed to enter the structure from the region $z > z_N$.

3. SOLUTION BY TRANSFER MATRICES

Let L be the extension of the computational domain in the x direction. By imposing L-periodic boundary conditions, we may expand the electric field and the permittivity into the Fourier series

$$\mathbf{e}(x, z) = e(x, z)\hat{\mathbf{y}} = \sum_m E^{(m)}(z) \exp(ik_x^{(m)}x)\hat{\mathbf{y}}, \qquad (12)$$

$$\epsilon(x, z) = \sum_m \epsilon^{(m)}(z) \exp(ik_x^{(m)}x), \qquad (13)$$

where $k_x^{(m)} = 2\pi m/L$. The Fourier components are given as

$$\epsilon^{(m)}(z) = \frac{1}{L} \int_0^L \epsilon(x, z) \exp(-ik_x^{(m)}x)\mathrm{d}x. \qquad (14)$$

By inserting the Fourier series into the Helmholtz equation, we obtain

$$\frac{d^2 E^{(m)}(z)}{dz^2} - (k_x^{(m)})^2 E^{(m)}(z) + k^2 \sum_{m'} \epsilon^{(m-m')}(z) E^{(m')}(z) = 0, \qquad (15)$$

for each m. Let $\mathbf{E} = \{E^{(m)}\}_{m \in \mathbb{Z}}$ and use $k^2 = (k_x^{(m)})^2 + (k_z^{(m)})^2$. We may then write Eq. (15) as the matrix equation

$$\frac{d^2\mathbf{E}(z)}{dz^2} + (\mathbf{k}_z^2 + \mathbf{V}(z))\mathbf{E}(z) = 0, \qquad (16)$$

where $\mathbf{k}_z = \mathrm{diag}(k_z^{(m)})$, and $\mathbf{V}(z)$ is the infinite dimensional Toeplitz matrix operator defined as

$$\mathbf{V}(z) = -k^2\mathbf{I} + k^2 \begin{bmatrix} \ddots & & \vdots & & \\ \cdots & \epsilon^{(0)} & \epsilon^{(-1)} & \epsilon^{(-2)} & \\ & \epsilon^{(1)} & \epsilon^{(0)} & \epsilon^{(-1)} & \\ & \epsilon^{(2)} & \epsilon^{(1)} & \epsilon^{(0)} & \cdots \\ & & & \vdots & \ddots \end{bmatrix}. \qquad (17)$$

Equation (16) may be decomposed into a first-order system by writing $\mathbf{E}(z) = \mathbf{E}^+(z) + \mathbf{E}^-(z)$ and requiring

$$\frac{d\mathbf{E}^+(z)}{dz} = i\mathbf{k}_z\mathbf{E}^+(z) + i(2\mathbf{k}_z)^{-1}\mathbf{V}(z)(\mathbf{E}^+(z) + \mathbf{E}^-(z)), \quad (18a)$$

$$\frac{d\mathbf{E}^-(z)}{dz} = -i\mathbf{k}_z\mathbf{E}^-(z) - i(2\mathbf{k}_z)^{-1}\mathbf{V}(z)(\mathbf{E}^+(z) + \mathbf{E}^-(z)). \quad (18b)$$

Equation (16) follows easily from Eqs. (18a) and (18b) after summation and differentiation. Note that, outside the structure, $\mathbf{V}$ equals zero, and the solutions to Eq. (18) are forward- and backward-going waves.

By writing

$$\Psi(z) = \begin{bmatrix} \mathbf{E}^+(z) \\ \mathbf{E}^-(z) \end{bmatrix},$$

$$\mathbf{C}(z) = \begin{bmatrix} i\mathbf{k}_z + i(2\mathbf{k}_z)^{-1}\mathbf{V}(z) & i(2\mathbf{k}_z)^{-1}\mathbf{V}(z) \\ -i(2\mathbf{k}_z)^{-1}\mathbf{V}(z) & -i\mathbf{k}_z - i(2\mathbf{k}_z)^{-1}\mathbf{V}(z) \end{bmatrix}, \quad (19)$$

Equation (18) can be brought into the compact matrix form

$$\frac{d\Psi(z)}{dz} = \mathbf{C}(z)\Psi(z). \qquad (20)$$

Since the permittivity is independent of z within a layer, the matrix $\mathbf{C}$ will be constant for each layer. Thus, Eq. (20) can be integrated to

$$\Psi(z_b) = \exp[(z_b - z_a)\mathbf{C}]\Psi(z_a) \qquad (21)$$

for z_a and z_b inside the same layer. Let $\mathbf{C}_i$ be the $\mathbf{C}$ matrix for layer i. By defining

$$\mathbf{M}_i = \exp(\Delta_i \mathbf{C}_i), \qquad (22)$$

we obtain

$$\Psi(z_i) = \mathbf{M}_i \Psi(z_{i-1}). \qquad (23)$$

Since e and $\partial e / \partial z$ are continuous across the layer boundaries, $\mathbf{E}^+$ and $\mathbf{E}^-$ also must be continuous here. By successive applications of Eq. (23), we are able to propagate through the structure from z_0 to z_N,

$$\Psi(z_N) = \prod_{i=N}^{0} \mathbf{M}_i \Psi(z_0) = \mathbf{M}\Psi(z_0). \qquad (24)$$

The boundary conditions at $z = z_0 = 0$ are contained in

$$\Psi(z_0) = \begin{bmatrix} \mathbf{E}^+(z_0) \\ \mathbf{E}^-(z_0) \end{bmatrix}, \qquad (25)$$

where $\mathbf{E}^+(z_0)$ is given by the probing waves, and $\mathbf{E}^-(z_0)$ is unknown. At the other end of the structure,

$$\Psi(z_N) = \begin{bmatrix} \mathbf{E}^+(z_N) \\ 0 \end{bmatrix}, \qquad (26)$$

where $\mathbf{E}^+(z_N)$ has to be determined. If we partition the matrix $\mathbf{M}$ according to the definition of Ψ,

$$\mathbf{M} = \begin{bmatrix} \mathbf{M}_{11} & \mathbf{M}_{12} \\ \mathbf{M}_{21} & \mathbf{M}_{22} \end{bmatrix}, \qquad (27)$$

and consider the matrix equation

$$\begin{bmatrix} \mathbf{E}^+(z_N) \\ 0 \end{bmatrix} = \begin{bmatrix} \mathbf{M}_{11} & \mathbf{M}_{12} \\ \mathbf{M}_{21} & \mathbf{M}_{22} \end{bmatrix} \begin{bmatrix} \mathbf{E}^+(z_0) \\ \mathbf{E}^-(z_0) \end{bmatrix}, \qquad (28)$$

the formal solution is easily seen to be

$$\mathbf{E}^-(z_0) = \mathbf{R}\mathbf{E}^+(z_0), \qquad (29)$$

$$\mathbf{E}^+(z_N) = \mathbf{T}\mathbf{E}^+(z_0), \qquad (30)$$

where $\mathbf{R}$ and $\mathbf{T}$ are the so-called *reflection* and *transmission matrices* for the structure

$$\mathbf{R} = -\mathbf{M}_{22}^{-1}\mathbf{M}_{21}, \qquad (31)$$

$$\mathbf{T} = \mathbf{M}_{11} - \mathbf{M}_{12}\mathbf{M}_{22}^{-1}\mathbf{M}_{21}. \qquad (32)$$

The reflection and transmission matrices provide $\mathbf{E}^-(z_0)$ and $\mathbf{E}^+(z_N)$ for all possible input $\mathbf{E}^+(z_0)$.

To solve the inverse problem, we need reflectance data for all possible incident wavenumbers. Such a set of excitation–response pairs can be described by the following equation:

$$\begin{bmatrix} \mathbf{T} \\ 0 \end{bmatrix} = \mathbf{M} \begin{bmatrix} \mathbf{I} \\ \mathbf{R} \end{bmatrix}. \qquad (33)$$

Here each column i of $\mathbf{I}$ corresponds to an experiment where the incident field amplitude is 1 for one of the Fourier components and 0 for the others. The ith column of $\mathbf{R}$ is the

reflection at z_0, and the ith column of $\mathbf{T}$ is the corresponding transmission at z_N.

4. INVERSE PROBLEM

The inverse problem is solved by combining reflectance data for a range of frequencies, $[\omega_1, \omega_2]$, so as to synthesize data from a short pulse at the time the pulse hits the surface. The permittivity of the layer may then be recovered as described below if the pulse width in time, $\mathcal{O}(2\pi(\omega_2 - \omega_1)^{-1})$, is shorter than the round-trip travel time in the layer, $2\Delta_i/c$. In this study we shall, for simplicity, assume that the layer thicknesses, Δ_i, are known. It is, in principle, possible to do the layer stripping without knowledge of the layer thickness. This will be briefly discussed in Section 6. From the permittivity and the thickness it is now possible to compute the transfer matrix for the layer and remove the impact of the layer from the reflection data. Thus, we obtain reflectance data for the same structure, but without the leftmost layer, and may then repeat the steps above until the entire structure has been reconstructed.

A. Computing the Permittivity

Let us assume that we have reflectance data from an experiment where the incident wave is a plane wave pulse, $F(t - z/c_0)$; see Fig. 1. The incident wave enters from $z < 0$ and first hits the leftmost layer of the structure. The wave speed in the first layer is $c_1(x)$.

Let us consider a small neighborhood around the point x and assume that the permittivity in the leftmost layer is varying slowly enough so that we may take it to be constant and equal to $\epsilon_1(x)$ inside the area we consider. Furthermore, we restrict our calculation to a small time interval so that the reflected and transmitted waves are only affected by the first layer.

At the left side of the boundary, the electric field will be a sum of the incoming and the reflected wave, and at the right side, the field consists of the transmitted wave. Thus, continuity of the transverse electromagnetic fields gives us
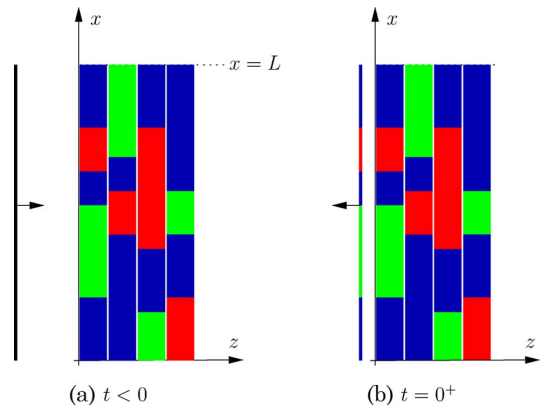

(a) $t < 0$ (b) $t = 0^+$

Fig. 1. (Color online) (a) A plane wave pulse is incident to a layered 2D structure. For the structure, different colors indicate different refractive indices. (b) Immediately after $t = 0$, the field has only been affected by the first layer; thus, we may identify the first layer from the first part of the reflected field in the time domain.

$$F\left(t - \frac{z}{c_0}\right) + R_1(x)F\left(t + \frac{z}{c_0}\right) = T_1(x)F\left(t - \frac{z}{c_1(x)}\right), \quad (34)$$

$$-\frac{1}{c_0}F'\left(t - \frac{z}{c_0}\right) + \frac{R_1(x)}{c_0}F'\left(t + \frac{z}{c_0}\right) = -\frac{T_1(x)}{c_1(x)}F'\left(t - \frac{z}{c_1(x)}\right),$$
$$(35)$$

for some reflection coefficient $R_1(x)$. Obviously, the incident wave pulse F needs to be short for Eqs. (34) and (35) to hold. For $z = 0$ and $0 \leq t \ll \Delta_1/c_0$, we thus have from Eqs. (34) and (35)

$$1 + R_1(x) = T_1(x), \quad (36)$$

$$-1 + R_1(x) = -T_1(x)\frac{c_0}{c_1(x)}, \quad (37)$$

leading to the following expression for the permittivity in the leftmost layer:

$$\epsilon_1(x) = \epsilon_0\left(\frac{1 - R_1(x)}{1 + R_1(x)}\right)^2. \quad (38)$$

Equation (38) can be interpreted as a local Fresnel equation; it connects the local reflection coefficient $R_1(x)$ and the local permittivity $\epsilon_1(x)$.

B. Layer Stripping

For the layer stripping we shall assume that the layer thickness is known. Once we have computed $\epsilon_1(x)$, we obtain the transfer matrix $\mathbf{M}_1$ from Eq. (22). As in Eq. (23), the forward- and backward-going waves just before the second layer can be computed as

$$\begin{bmatrix} \mathbf{E}^+(z_1) \\ \mathbf{E}^-(z_1) \end{bmatrix} = \mathbf{M}_1 \begin{bmatrix} \mathbf{E}^+(z_0) \\ \mathbf{E}^-(z_0) \end{bmatrix} = \mathbf{M}_1 \begin{bmatrix} \mathbf{I} \\ \mathbf{R} \end{bmatrix}. \quad (39)$$

Note that here $\mathbf{E}^+$ and $\mathbf{E}^-$ are matrices as in Eq. (33). Similar to the solution for the full structure, Eqs. (29) and (30), we may define

$$\mathbf{E}^+(z_N) = \tilde{\mathbf{T}}\mathbf{E}^+(z_1), \quad (40)$$

$$\mathbf{E}^-(z_1) = \tilde{\mathbf{R}}\mathbf{E}^+(z_1), \quad (41)$$

and thus the new reflection matrix can be found as

$$\tilde{\mathbf{R}} = \mathbf{E}^-(z_1)\mathbf{E}^+(z_1)^{-1}. \quad (42)$$

5. ALGORITHM

For the numerical experiments, which we will discuss in Section 6, we first solve the forward problem to obtain valid reflectance data $\mathbf{R}(k_x^{(m')}, k_x^{(m)}, \omega)$ for each of N_ω frequencies in the span $[\omega_1, \omega_2]$. Here $k_x^{(m')}$ denote the incident wavenumbers, and $k_x^{(m)}$ the reflected wavenumbers.

For the inverse problem, the first step is to synthesize a time-localized pulse in space and time to be applied in Eq. (38). Only data for incident waves normal to the structure are used in the identification of the layers. We start with a transformation from $k_x^{(m)}$ to x,

$$r(x, \omega) = \sum_m \mathbf{R}(k_x^{(m')} = 0, k_x^{(m)}, \omega)e^{ik_x^{(m)}x}, \quad (43)$$

where

$$k_x^{(m)} = \frac{2\pi m}{L}, \qquad m \in \mathbb{Z}, \quad \text{and} \quad \omega \in [\omega_1, \omega_2]. \quad (44)$$

Ideally, one would now carry out an inverse Fourier transform in order to obtain the reflected field in the space and time domains resulting from an incident delta pulse,

$$R(x, t) = \frac{1}{2\pi}\int_{-\infty}^{\infty} r(x, \omega)e^{-i\omega t}d\omega. \quad (45)$$

However, since we only know $r(x, \omega)$ in the frequency interval $[\omega_1, \omega_2]$, we need to choose a window function $W(\omega)$ with support in that interval. The corresponding pulse in time is denoted $w(t)$, and the experience with some standard window functions are discussed in Section 6. The synthetic response will then be

$$R_w(x, t) = \frac{1}{2\pi}\int_{\omega_1}^{\omega_2} r(x, \omega)W(\omega)e^{-i\omega t}d\omega. \quad (46)$$

For $z = 0$ and $0 \leq t \ll \Delta_1$, we see from Eq. (34) that $R_w(x, t) = R_1(x)w(t)$. Hence, for $t = 0$, we may write

$$R_1(x) = \frac{R_w(x, 0)}{w(0)} = \frac{\int_{\omega_1}^{\omega_2} r(x, \omega)W(\omega)d\omega}{\int W(\omega)d\omega}. \quad (47)$$

The permittivity $\epsilon(x)$ is then obtained from Eq. (38). The layer stripping has been discussed in Section 4.B.

The numerical method may now be summarized in a pseudo code, as follows.

Input to the algorithm: reflection matrices $\mathbf{R}(k_x^{(m')} = 0, k_x^{(m)}, \omega)$, for $\omega \in [\omega_1, \omega_2]$.

1. Transform reflection matrices to the space/frequency domain using Eq. (43). Next, determine the reflection coefficient at $t = 0$ using Eq. (47). The permittivity now follows from Eq. (38).
2. Use $\epsilon(x)$ and Eq. (14) to find the Fourier components. Then the transfer matrix can be computed from Eqs. (17), (19), and (22).
3. Knowing the transfer matrix, the forward- and backward-going waves before the next layer can be computed from Eq. (39).
4. Compute the new reflection matrix, using Eq. (42).
5. Return to step 1 to compute the permittivity in the next layer until all layers have been found.

6. NUMERICAL EXPERIMENTS

For simplicity, we scale ϵ_0 and μ_0 (in free space) to 1, and hence $c_0 = 1$. Now the dispersion relation in free space reduces to $k = \omega$ and the wavelengths will be $\lambda = 2\pi/\omega$. The length of the synthesized pulse will depend on the frequency interval $[\omega_1, \omega_2]$ and be of order $2\pi(\omega_2 - \omega_1)^{-1}$. One must require that the pulse length is shorter than the round-trip travel time in the first layer, i.e.,

$$\frac{2\pi}{\omega_2 - \omega_1} \lesssim \frac{2\Delta_1}{c_1}. \quad (48)$$

Thus, to be able to reconstruct the structure, we need to make sure that the frequency band is wide enough. Through

simulations we have seen that, for smaller frequency bands, the error fluctuates as the bandwidth grows. However, as soon as the frequency span is wide enough, the calculations are stable.

As mentioned in Section 5, we use Eq. (33) to compute reflection matrices for the forward problem. To compute the reflection matrix and solve the inverse problem, the number of Fourier components, M, the computational domain, L, and the N_ω frequencies in the interval $[\omega_1, \omega_2]$ must be chosen. Now the reflection and transmission matrices will have dimension $M \times M$, and the propagation matrix **M** dimension $2M \times 2M$. Note that, given the resolution in the x direction,

$$\Delta x = \frac{L}{M}, \tag{49}$$

the maximum Nyquist wavenumber is given as

$$\max k_x = \frac{\pi M}{L}. \tag{50}$$

Since

$$k_z = \sqrt{k^2 - k_x^2} = \sqrt{\omega^2 - k_x^2}, \tag{51}$$

evanescent modes in vacuum occur when $\max k_x > \omega$.

As we see in Eq. (42), the updated reflection matrix is a product of the backward-traveling waves and the inverse of the forward-traveling waves. In a homogeneous medium, the forward- and backward-traveling waves have the z dependence $\exp(ik_z z)$ and $\exp(-ik_z z)$, respectively. Thus, when we have evanescent modes with $k_z = iK$ for some $K > 0$, we expect a noise amplification factor of the order of $\exp(2K\Delta)$ when one layer is stripped off. Because of this, we restrict our frequency band to avoid a too large K.

Note that, if the variations in the x direction are fast, we will need a finer resolution in x. To obtain this, we must either make M larger or L smaller, which again implies that the maximum wavenumber, $\max k_x$, increases. The result is that we need higher frequencies to avoid evanescent modes. Thus, it is convenient to restrict the attention to structures that vary slowly with respect to x. We will, however, in Example 2 (see Section 6.B), see that we are also able to reconstruct a structure with fast variations.

There are three effects that mainly contribute to the limitations in this method. The first one is the effect of evanescent modes, which was discussed in this section. The second is related to the contrast between the minimum and maximum refractive indices, n_1 and n_2. As the contrast grows higher, more of the light is reflected by the first layers. This will in turn make the calculations less accurate [8,9]. The last effect is also related to the bandwidth. As discussed in the beginning of this section, we need the pulse length to be smaller than the layer round-trip travel time, thus imposing a lower limit to the bandwidth. Conversely, if the bandwidth is fixed, the layer thicknesses have to be large enough.

As discussed in Section 5, it is necessary to shape the reflection data using some window function. Numerical experiments applying three different window functions on the interval $[\omega_1, \omega_2]$ are presented in Section 6.A. As expected, the experiments favor smoother windows over the simple rectangular window. Consequently, a Hanning window has been applied for the rest of the computations.

In all simulations we have assumed that we know the layer thickness. It would, at least in principle, be possible to reconstruct the layer thickness. To do this, one needs to use a fictitious layer thickness, Δz, which must be small compared to the expected layer thickness. Then this Δz can be used in the computations, to reconstruct each layer piece by piece.

All the calculations where done using MATLAB on an Intel Core 2 Quad 2.83 GHz computer. For a typical calculation, the runtime was approximately 260 s. About 180 s was used on calculating the forward problem, i.e., the reflection matrices $\mathbf{R}(k_x^{(m')}, k_x^{(m)}, \omega)$, the calculation of the permittivity is neglectable, and the calculation and removal of the leftmost layer took about 80 s.

A. Example 1

In this example we have chosen a structure where the permittivity within the layers is given as

$$\epsilon(x) = \eta \pm \gamma \cos\left(\frac{x}{2}\right), \tag{52}$$

and where the two different layers are obtained by alternating between $+$ and $-$. The layer thickness has been set to $\pi/2$, and
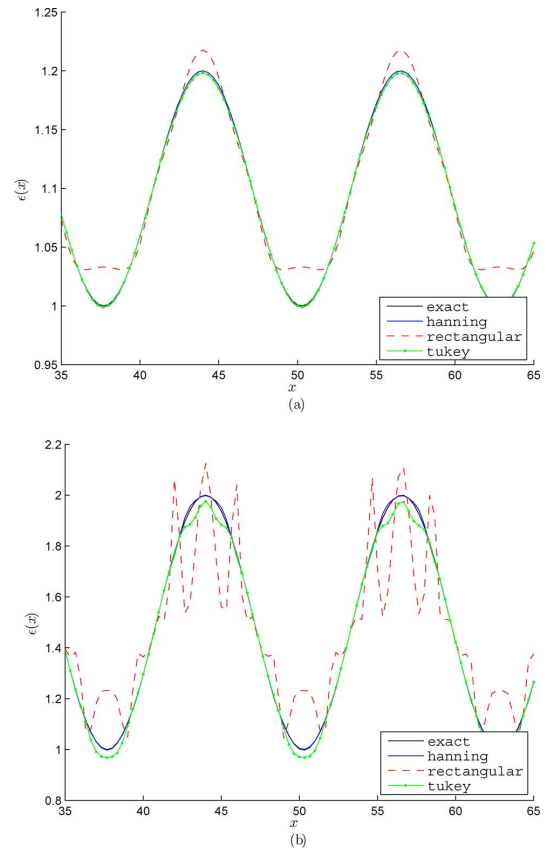

Fig. 2. (Color online) Reconstruction of the second layer for different window functions, in (a) $n_2^2 = 1.2$ and in (b) $n_2^2 = 2.0$. Other parameters: $M = 300$, $L = 100$, $N_\omega = 100$, $\omega \in [9, 19]$, $\Delta z = \pi/2$, $n_1^2 = 1.0$. Note that only parts of the computational domain L are shown in the plots.

the parameters η and γ are chosen so that

$$\min \epsilon = n_1^2 = 1.0, \qquad (53)$$

$$\max \epsilon = n_2^2, \qquad (54)$$

i.e., n_1 is kept constant, while n_2^2 is varied. For all the experiments presented here, $M = 300$ and $L = 100$, giving a resolution in x of $1/3$ and a maximum k_x of 3π. The choice of frequency band depends on whether we want to include evanescent modes in the computations, how large K we can tolerate, and the layer thickness.

We first consider the choice of frequency window functions, Eq. (46), by testing three different functions: a simple rectangular window, the Hanning window, and the Tukey (tapered cosine) window. The comparisons were carried out for two different values of n_2: $n_2^2 = 1.2$ for the first test, and $n_2^2 = 2.0$ for the second. The real difference in the choice of window functions can only be seen in the reconstruction of the second layer. Therefore, the results, displayed in Fig. 2, are shown for only this layer. The rectangular window give poor results already for the lowest refractive index, whereas the two other choices give a nice reconstruction. For the higher index, we see that the Tukey window is also beginning to give less ac-

curate results, while for the Hanning window there is almost no visible difference from the exact curve. For the rest of the numerical examples, we have therefore chosen to use the Hanning window.

Let us now turn to the effect of including evanescent modes. In these experiments, the permittivity was first chosen such that $n_1^2 = 1.0$ and $n_2^2 = 1.05$, and secondly, we had $n_1^2 = 1.0$ and $n_2^2 = 2.0$. The frequency bandwidth was set constant to 10, but the lower and upper frequencies were changed to include none, or some evanescent modes. Again, the first layer is nicely reconstructed, so we only show results for the second layer in Fig. 3. Including some evanescent modes improves the results, but if K gets too large, there are fluctuations in the reconstruction. Note that, as n_2 gets higher, a larger K is acceptable. This can be explained by the fact that the field now is locally nonevanescent, since a local k_z in the medium would be $k_z = (n^2\omega^2 - k_x^2)^{1/2}$.

Bigger contrasts in the refractive index may be simulated by keeping the lower index constant at $n_1^2 = 1.0$ while the upper index is changed. The results are shown in Fig. 4, and we see that the first layer is well reconstructed for all choices of n_2^2, while some fluctuations in the second layer are visible when $n_2^2 > 2$.
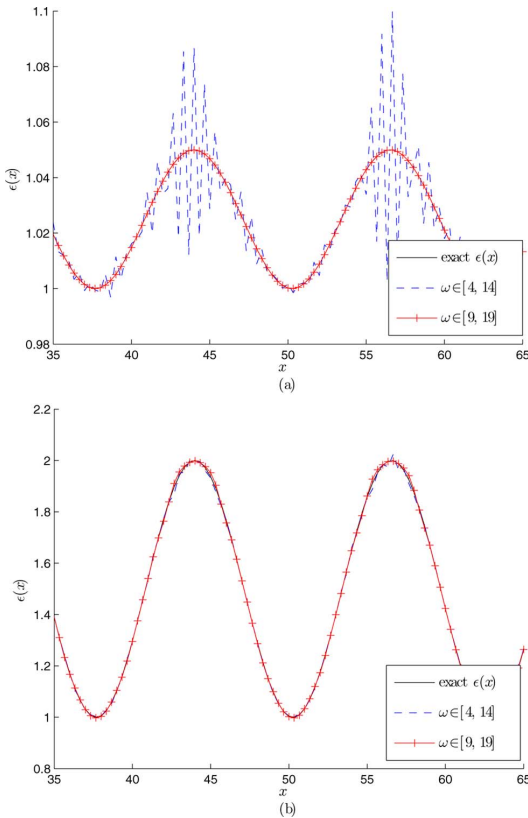

Fig. 3.   (Color online) Reconstruction of the second layer for different ω_1 and ω_2, but with constant bandwidth. In (a) $n_2^2 = 1.05$, and in (b) $n_2^2 = 2.0$. Other parameters: $M = 300$, $L = 100$, $N_\omega = 100$, $\Delta z = \pi/2$, $n_1^2 = 1.0$.
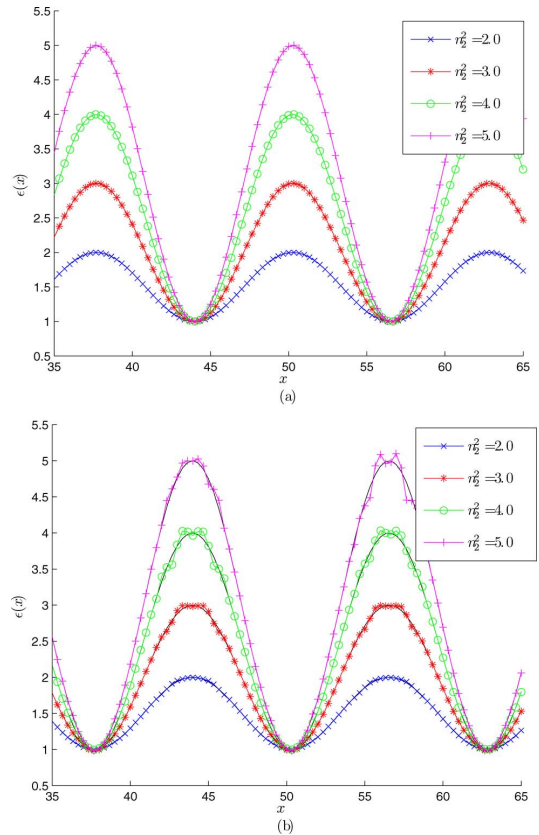

Fig. 4.   (Color online) Reconstruction of (a) the first layer, and (b) the second layer, for different choices of n_2. Other parameters: $M = 300$, $L = 100$, $\omega \in [9, 19]$, $N_\omega = 100$, $\Delta z = \pi/2$, $n_1^2 = 1.0$. The solid black lines represent the exact permittivity.
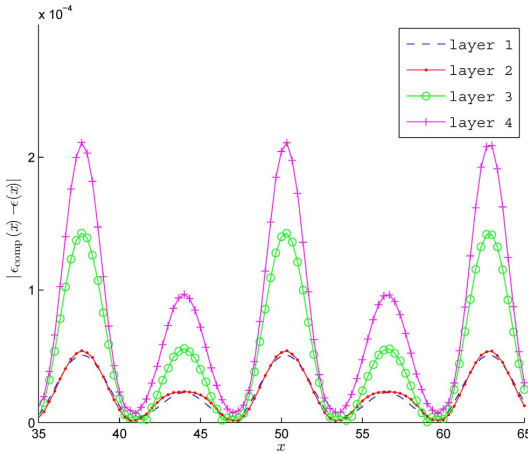
Fig. 5. (Color online) Error in each layer, given as $|\epsilon_{comp} - \epsilon|$. Parameters: $M = 300$, $L = 100$, $\omega \in [9, 19]$, $N_\omega = 100$, $\Delta z = \pi/2$, $n_1^2 = 1.0$, $n_2^2 = 1.05$.

Finally, we demonstrate that it is possible to reconstruct more than two layers. Figure 5 shows the error, given as $|\epsilon_{comp} - \epsilon|$, for each layer in a structure consisting of four
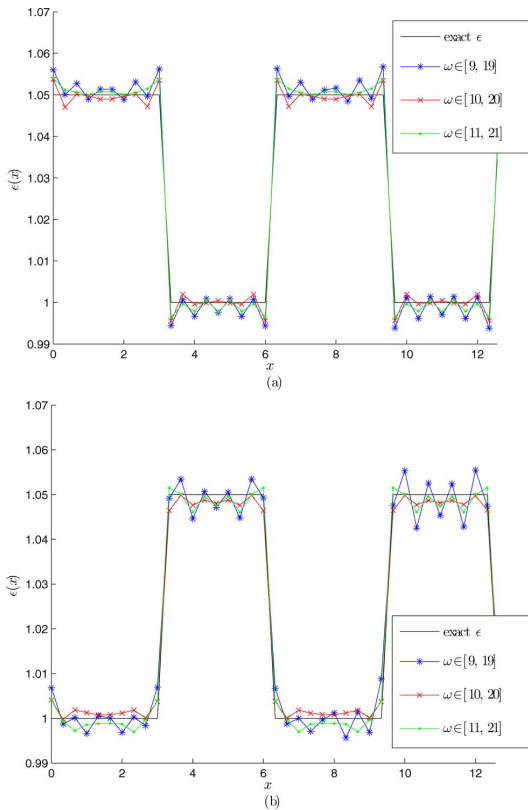

Fig. 6. (Color online) Reconstruction of the square function (a) for the first layer, and (b) for the second layer. The computations were done for different ω_1 and ω_2, but with constant bandwidth. Other parameters: $M = 300$, $L = 100$, $N_\omega = 100$, $\Delta z = \pi/2$, $n_1^2 = 1.0$, $n_2^2 = 1.05$.

layers. The permittivity was chosen between $n_1^2 = 1.0$ and $n_2^2 = 1.05$.

B. Example 2: A Square Function

In this example we have chosen the permittivity to be a square function with period 2π in each layer. To get two different layers and a permittivity between n_1 and n_2, we let

$$\epsilon_1(x) = \begin{cases} n_2^2, & 0 \le x < \pi \\ n_1^2, & \pi \le x < 2\pi \end{cases}, \tag{55}$$

$$\epsilon_2(x) = \begin{cases} n_1^2, & 0 \le x < \pi \\ n_2^2, & \pi \le x < 2\pi \end{cases}. \tag{56}$$

This example has been chosen to show that we are able to reconstruct a less smooth function. The fact that the permittivity changes fast seems to be in conflict with the discussion in Section 6, but, as we see from Fig. 6, we actually manage to reconstruct two layers of this structure as well. The reason it works is that we only use the low-frequency components of the square. The results can be seen in Fig. 6.

7. CONCLUSION

In this paper we have presented a method for reconstructing 2D photonic structures layer by layer. In principle, the reconstruction is exact, and we have shown through numerical examples that we are able to reconstruct different structures consisting of several layers.

There are essentially three fundamental mechanisms that limit the accuracy in practice: the presence of evanescent modes, accumulated reflection, and limited bandwidth. The fact that evanescent modes lead to inaccuracies means that either the probing frequencies must be sufficiently high or the spatial transversal frequencies of the structure must be sufficiently small. The second limitation is a result of the fact that, if the transmission through the structure is too small, little light reaches the back end. Then the back end has little influence on the reflection data and cannot be reconstructed accurately. Finally, the bandwidth must be sufficiently large such that the synthetic incident pulse is shorter than the round-trip time in all layers. Alternatively, for a fixed, available bandwidth, the structure must vary sufficiently slowly in the longitudinal direction z. In the numerical examples, for a center wavelength $1\,\mu m$, the normalized frequency interval $[9, 19]$ corresponds to the wavelength interval $[0.74, 1.56]\,\mu m$. The layer thicknesses in the example become $3.5\,\mu m$. If the available bandwidth is reduced to $100\,nm$, the layers must be 5–10 times thicker to achieve the same accuracy.

REFERENCES

1. E. Yablonovitch, "Inhibited spontaneous emission in solid-state physics and electronics," Phys. Rev. Lett. **58**, 2059–2062 (1987).
2. S. John, "Strong localization of photons in certain disordered dielectric superlattices," Phys. Rev. Lett. **58**, 2486–2489 (1987).
3. J. D. Joannopoulos, R. D. Meade, and J. N. Winn, *Photonic Crystals: Molding the Flow of Light* (Princeton University, 1995).
4. A. M. Bruckstein, B. C. Levy, and T. Kailath, "Differential methods in inverse scattering," SIAM J. Appl. Math. **45**, 312–335 (1985).
5. A. E. Yagle and B. C. Levy, "Layer-stripping solutions of multidimensional scattering problems," J. Math. Phys. **27**, 1701–1710 (1986).

6. J. Skaar, L. Wang, and T. Erdogan, "On the synthesis of fiber Bragg gratings by layer peeling," IEEE J. Quantum Electron. **37**, 165–173 (2001).

7. O. H. Waagaard and J. Skaar, "Inverse scattering in multimode structures," SIAM J. Appl. Math. **68**, 311–333 (2007).

8. A. M. Bruckstein, I. Koltracht, and T. Kailath, "Inverse scattering with noisy data," SIAM J. Sci. Statist. Comput. **7**, 1331–1349 (1986).

9. J. Skaar and R. Feced, "Reconstruction of gratings from noisy reflection data," J. Opt. Soc. Am. A **19**, 2229–2237 (2002).

Paper III

Adaptive algorithm for an inverse electromagnetic scattering problem

L. Beilina, M. P. Hatlo and H. E. Krogstad

Applicable Analysis, Vol. 88, No. 1, pp. 15–28, January 2009

Paper IV

Reconstruction of dielectrics in a symmetric structure via adaptive algorithm with backscattering data

L. Beilina, M. P. H. Andresen and H. E. Krogstad